

Two codependent routes lead to high-level MRSA

ADEDEJI-OLULANA, Abimbola Feyisara, WACNIK, Katarzyna, LAFAGE, Lucia, PASQUINA-LEMONCHE, Laia, TINAJERO-TREJO, Mariana, SUTTON, Joshua A.F., BILYK, Bohdan, IRVING, Sophie E., PORTMAN ROSS, Callum J., MEACOCK, Oliver J., RANDERSON, Sam A., BEATTIE, Ewan, OWEN, David S <<http://orcid.org/0000-0003-4989-8790>>, FLORENCE, James, DURHAM, William M., HORNBY, David P., CORRIGAN, Rebecca M, GREEN, Jeffrey, HOBBS, Jamie K. and FOSTER, Simon J.

Available from Sheffield Hallam University Research Archive (SHURA) at:

<https://shura.shu.ac.uk/34760/>

This document is the Accepted Version [AM]

Citation:

ADEDEJI-OLULANA, Abimbola Feyisara, WACNIK, Katarzyna, LAFAGE, Lucia, PASQUINA-LEMONCHE, Laia, TINAJERO-TREJO, Mariana, SUTTON, Joshua A.F., BILYK, Bohdan, IRVING, Sophie E., PORTMAN ROSS, Callum J., MEACOCK, Oliver J., RANDERSON, Sam A., BEATTIE, Ewan, OWEN, David S, FLORENCE, James, DURHAM, William M., HORNBY, David P., CORRIGAN, Rebecca M, GREEN, Jeffrey, HOBBS, Jamie K. and FOSTER, Simon J. (2024). Two codependent routes lead to high-level MRSA. *Science*, 386 (6721), 573-580. [Article]

Copyright and re-use policy

See <http://shura.shu.ac.uk/information.html>

Two co-dependent routes lead to high-level MRSA

Abimbola Feyisara Adedeji-Olulana^{1†}, Katarzyna Wacnik^{2,3,†}, Lucia Lafage^{2,3}, Laia Pasquina-Lemonche^{1,3}, Mariana Tinajero-Trejo^{2,3}, Joshua A. F. Sutton^{2,3}, Bohdan Bilyk^{2,3}, Sophie E. Irving^{2,3}, Callum J. Portman Ross^{2,3}, Oliver J. Meacock¹, Sam A. Randerson¹, Ewan Beattie¹, David S. Owen^{2‡}, James Florence^{2,3}, William M. Durham¹, David P. Hornby^{2,3}, Rebecca M. Corrigan^{2,3,4}, Jeffrey Green^{2,3}, Jamie K. Hobbs^{1,*}, Simon J. Foster^{2,3,*}

¹ Department of Physics and Astronomy, University of Sheffield, Sheffield, UK.

² School of Biosciences, University of Sheffield, Sheffield, UK.

³ The Florey Institute, University of Sheffield, Sheffield, UK.

⁴ School of Medicine, University College Dublin, Dublin, Ireland.

[†] These authors contributed equally to this work.

[‡] Present address. Department of Biosciences and Chemistry, Sheffield Hallam University, UK.

* Corresponding author. Email : jamie.hobbs@sheffield.ac.uk; s.foster@sheffield.ac.uk.

One Sentence Summary

High-level resistance in MRSA requires two pathways that reveal a novel cell division mode.

Abstract

Methicillin resistant *S. aureus* (MRSA) is of major clinical concern, in which acquisition of *mecA*, encoding the cell wall peptidoglycan biosynthesis component Penicillin Binding Protein 2a (PBP2a), confers resistance to β -lactam antibiotics. In the presence of antibiotics we show that MRSA adopts an alternative cell division mode, with altered peptidoglycan architecture at the division septum. PBP2a can replace the transpeptidase activity of the endogenous and essential PBP2, but not that of PBP1, which is responsible for the distinctive native septal peptidoglycan architecture. Successful division without PBP1 activity, requires the alternative division mode and is enabled by several possible chromosomal, potentiator (*pot*) mutations. MRSA resensitizing agents differentially interfere with the two co-dependent mechanisms required for high-level antibiotic resistance, providing opportunities for new interventions.

Introduction

Antibiotics are at the heart of modern medicine, but their efficacy is increasingly challenged by the spread of antimicrobial resistance (AMR) (1). MRSA is a so-called AMR “superbug”, that causes over 120,000 deaths per annum (2). Methicillin was introduced to circumvent clinical β -lactamase-mediated resistance, but soon became compromised due to the spread of MRSA (3). Resistance in MRSA is primarily based on the acquisition of the *mecA* gene encoding a novel PBP, named PBP2a, characterised by its low affinity for a broad range of β -lactams (3, 4). The *mecA* gene is carried on a mobile genetic element, the staphylococcal cassette chromosome (SCC*mec*) (3). SCC*mec* elements are classified into several types, including I, II, and III, which are primarily hospital-associated clones, and types IV and V often identified in community-associated MRSA (3).

PBPs are enzymes that carry out the final stages of assembly of bacterial cell wall peptidoglycan (PG). Cell wall PG is essential for viability of most bacteria and forms a single macromolecule around the cell (the sacculus), made of glycan strands and cross-linked via peptide side-chains (5). High resolution Atomic Force Microscopy (AFM) has recently revealed *S. aureus* PG to be a porous, heterogeneous hydrogel (6). Its mature surface is an open, disordered mesh with pores that penetrate deep into the wall, whereas the inner surface, where PG is synthesised, is a much denser mesh (6). Another feature of the PG is an outer architecture of concentric rings consisting of long glycan strands that is revealed upon cell scission and is characteristic of the newly exposed septum (6).

S. aureus has four endogenous PBPs of which only PBP1 and 2 are essential for PG synthesis, being able to carry out all the transpeptidase (linking side-chains) functions necessary for cell growth and division (7, 8, 9). PBP1 has multiple roles in cell division, by acting as a coordinator, through interactions with PG and divisome protein partners, and by providing the transpeptidase activity that is thought to be required for the characteristic ring architecture in septal PG (6, 7, 8).

PBP2a is a non-native enzyme in MRSA, acquired from an environmental source, so how it facilitates high-level antibiotic resistance by replacing the transpeptidase activity of endogenous PBPs is intriguing. PBP2a requires the transglycosylase activity of PBP2 to mediate resistance and the two proteins interact, thus demonstrating their functional cooperativity (10). PBP2a can maintain transpeptidase activity with a closed active site conformation, thus resisting β -lactam binding while interaction with a second PG substrate molecule at an allosteric site leads to a conformational change that opens the active site for catalysis (11).

An interesting feature of many clinical MRSA isolates is that they exhibit heterogeneous resistance, whereby only a very small proportion ($<10^{-4}$) of the population are high-level resistant ($>50 \mu\text{g ml}^{-1}$ methicillin) (12). Antibiotics can induce the conversion of the population to homogeneous high-level resistance, that does not revert in the absence of antibiotics. Chromosomal mutations that lead to the conversion to homogeneous resistance, mostly map to genes responsible for the regulation of aspects of cellular physiology and not PBP2a function directly (13). We have named these genes “potentiators” (*pot*), to differentiate them from auxiliary genes (*aux*), in which mutation leads to decreased resistance (13). We have recently carried out a directed evolution study that provides matched strains enabling the exploration of MRSA resistance mechanisms (14). Development of high-level MRSA is a two-step process whereby the presence of *mecA* is essential but in itself only results in a modest increase in minimum inhibitory concentration (MIC) (low-level MRSA). Acquisition of missense mutations in genes encoding RNA polymerase subunits (*rpoB* or *rpoC*), so-called *rpo** mutations, potentiate a step-change in resistance levels (high-level MRSA), both in the clinical environment and under laboratory conditions (13, 14).

Cell wall architecture of MRSA

AFM was used to analyse the nanoscale, PG architecture, where in all cases at least 20 individual sacculi (i.e. purified cell wall fragments) were examined (see Materials and Methods). AFM analysis (Fig. 1A-B; and fig. S1A-B and S2A-B) showed that low-level resistant MRSA (SH1000 *mecA*⁺ (hereafter designated *mecA*⁺); MIC $2 \mu\text{g ml}^{-1}$), in the absence of methicillin, resembled its sensitive parent (SH1000; MIC $0.25 \mu\text{g ml}^{-1}$). In both cases, the inner surface of the cell wall in all areas consisted of a dense mesh of PG, the outer surface of the septum, newly exposed after division, exhibited the characteristic septal PG concentric-ring architecture, and the PG at the outer surface of the cell, away from the most recent site of

division, consisted of an open mesh structure (6) (Fig. 1A-B; and fig. S1A-B, S2A-B). We quantified the orientation of individual glycan strands for strains SH1000 and *mecA*⁺ in the absence of antibiotic using a custom-made automated image analysis. This revealed that in both cases the outer surface of the septum exhibited a prominent peak in the circumferential direction that is consistent with the concentric-ring architecture (Fig. 1Aiii, Biii). However, no PG concentric rings were apparent at the outer surface of the septum of *mecA*⁺ in the presence of 1.5 $\mu\text{g ml}^{-1}$ methicillin (sub-MIC for *mecA*⁺). Rather, the outer surface of the septum appeared as a dense mesh structure (Fig. 1Di-iii), while the inner surface displayed a large proportion of long glycan strands that were oriented near the septal centre (fig. S1Dii, see the long orange-brown coloured-fibres in fig. S1Diii). Furthermore, the cell wall was thinner after treatment with methicillin (fig. S1F). Under the same conditions (1.5 $\mu\text{g ml}^{-1}$ methicillin), the parental strain, SH1000, died and cell wall spanning holes were apparent (15) (fig. S2F-H). The cell wall architecture of the high-level MRSA strain (SH1000 *mecA*⁺ *rpoB*^{*} (hereafter designated *mecA*⁺ *rpoB*^{*}); MIC $\geq 256 \mu\text{g ml}^{-1}$), which possessed both *mecA* and the *pot* mutation, *rpoB*^{*} coding for a variant of the RNA polymerase β subunit RpoB(H929Q) (14), resembled that of the parental strain (*mecA*⁺) in the absence of antibiotics (Fig. 1C; and fig. S1C and fig. S2C). When treated with 25 $\mu\text{g ml}^{-1}$ methicillin (sub-MIC for this strain but sufficient to kill both SH1000 and *mecA*⁺) the inner surface of the cell wall maintained a dense network of PG mesh, without the appearance of perforating holes (fig. S1Eii). However, in the large majority of cases, the septa were thickened with a distinct protuberance, or lump, at the centre (fig. S1Ei). Importantly, although *mecA*⁺ *rpoB*^{*} was able to grow and divide in the presence of methicillin, there was a total absence of the PG concentric-ring structure on the outer surface of newly divided cells (Fig. 1E). Septal PG concentric rings are a defining feature of PG architecture in several gram-positive bacteria (6, 16). Instead of PG concentric rings, the outer surface of septa obtained from methicillin-treated *mecA*⁺ *rpoB*^{*} consisted of a disordered, dense mesh with small pore size (Fig. 1E). As in the absence of antibiotics, the outer surface of the rest of the cell periphery appeared as a more open mesh with larger pore size (fig. S2E and S2I). This open mesh structure is derived from the dense mesh rather than from the concentric ring structure, which remodels as cells divide in different planes during subsequent division rounds (16). An interpretative diagram illustrating these observations is shown in Fig. 1F.

We then used the clinical, high-level, MRSA strain COL (SCC*mec* Type I), which possesses both the *mecA* gene and produces a variant RpoB(A798V, S875L) (14) (MIC $\geq 256 \mu\text{g ml}^{-1}$) to determine whether the resistance-associated PG architectural changes described above (absence of septal PG concentric rings, retention of PG dense mesh without perforating holes) are a common feature of MRSA cells under antibiotic stress. The COL cells were smaller than SH1000 (average cell volume 0.69 ± 0.14 vs $1.22 \pm 0.31 \mu\text{m}^3$) as were the cells of *mecA*⁺ *rpoB*^{*} (average cell volume $0.60 \pm 0.20 \mu\text{m}^3$, fig. S4D). Without antibiotics, COL displayed septal PG concentric rings (fig. S3A), whereas in the presence of 25 $\mu\text{g ml}^{-1}$ methicillin (sub-MIC), the septal PG of COL exhibited no concentric rings, but rather a disordered, dense mesh, at the septal outer surface (fig. S3G). Treatment of *mecA*⁺, *mecA*⁺ *rpoB*^{*} and COL with sub-MIC concentrations of antibiotics (1.5, 25, and 25 $\mu\text{g ml}^{-1}$, respectively) led to high levels of PG synthesis at the septum (as observed by ADA-DA incorporation), an increase in cell volume and septal abnormalities observed by fluorescence microscopy and transmission electron microscopy (TEM) (fig. S4).

To demonstrate the wider applicability of our findings we then analyzed representatives of different MRSA lineages and SCC*mec* types (SCC*mec* II (Mu50, MRSA252), III (TW20) and IV (USA300, EMRSA15)) (3, 17-20). All strains had methicillin MICs of $>256 \mu\text{g ml}^{-1}$ apart from EMRSA15 and USA300 (MIC 64 and 1-2 $\mu\text{g ml}^{-1}$, respectively) (Table S1). High-level

MRSA derivatives (MIC >256 µg ml⁻¹), of the latter two strains, designated USA300 (HL) and EMRSA15 (HL), were selected by directed evolution on oxacillin gradient plates (see Materials and Methods).

AFM analysis of the clinical strains and high-level resistant derivatives was carried out in the absence and presence of 25 µg ml⁻¹ methicillin (sub-MIC; fig. S3). All untreated strains had septal PG concentric rings at the outer face of the septum (fig. S3). In the presence of 25 µg ml⁻¹ methicillin (sub-MIC), the septal PG of COL, EMRSA15 (HL) and USA300 (HL) had a disordered, dense mesh, at the septal outer surface but Mu50, MRSA252 and TW20 had occasional (10 - 30% of septa) residual PG orientation. Growth of Mu50, MRSA252, and TW20 in 50 µg ml⁻¹ methicillin (sub-MIC) gave rise to disordered mesh at the septal outer surface (fig. S3). Thus, similar adaptations in septal PG architecture in response to antibiotic challenge are conserved across MRSA strains (Fig. 1F).

Thus, even though PBP2a, in MRSA backgrounds permits growth and division in the presence of antibiotics, it leads to profound changes to cell wall architecture. This raises the questions as to how PBP2a complements the loss of both essential PBP1 and PBP2 transpeptidase activities, and also how high-level MRSA is able to divide?

Mode of cell division underpins high-level MRSA

We have recently suggested that the *S. aureus* septal PG concentric rings are due to PBP1 transpeptidase activity (8). Methicillin sensitive *S. aureus* (MSSA) specifically lacking PBP1 transpeptidase activity is not viable and exhibits aberrant septa (8). However, a high-level MRSA strain with the same site-directed inactivation of PBP1 transpeptidase activity can grow (8), suggesting that PBP2a complements the lack of PBP1 activity, but perhaps without the ability to construct the septal PG concentric-ring structures. We therefore constructed a set of otherwise isogenic strains where, in the absence of the inducer IPTG, only PBP1 without transpeptidase activity (PBP1*) was expressed (Fig. 2A; and fig. S5A and B). Wholly unexpectedly, the presence of PBP2a in this background SH1000 *P_{spac}-pbp1 pbp1* mecA⁺* (hereafter designated *pbp1* mecA⁺*) did not complement the loss of PBP1 transpeptidase activity, demonstrating that PBP2a cannot substitute for the essential transpeptidase function of PBP1 (Fig. 2B). Conversely, a single point mutation in *rpoB* (resulting in amino acid replacement H929Q; *rpoB**), that is required for MRSA with high-level resistance (14), was able to entirely restore the ability of PBP1* to grow in the absence of PBP2a (Fig. 2B; and fig. S5C and D). Growth of *P_{spac}-pbp1 pbp1* rpoB** (hereafter designated *pbp1* rpoB**) without IPTG was associated with septal abnormalities, an increase in cell volume, and alterations to PG synthesis (Fig. 2C and D; and fig. S5E-F and S6A), similar to high-level MRSA grown in the presence of antibiotics (fig. S4B).

AFM analysis of the PG architecture of *pbp1* rpoB** with IPTG (PBP1 transpeptidase activity present) revealed open mesh on outer surfaces and septal PG concentric rings as expected for a wild type strain (Fig. 2E (+IPTG); Fig. S6B to D). However, growth without IPTG (no PBP1 transpeptidase activity) led to the concentric rings at the septal surface being replaced by a disordered, dense mesh with random glycan strand orientation (Fig. 2E (-IPTG); and fig. S6E to G). Although *rpoB** complemented the absence of PBP1 transpeptidase activity, neither *rpoB** nor PBP2a, or both combined, could rescue cells lacking the PBP1 protein (fig. S7), consistent with the physical presence of PBP1 being necessary for cell division complex assembly. Therefore, the septal PG ring architecture associated with conventional cell division requires the essential transpeptidase activity of PBP1, but *S. aureus* can adopt an alternative division mode facilitated by *rpoB** when PBP1 transpeptidase activity is lost (either by mutation or antibiotic addition; Fig. 1F). This fundamentally different mode of cell division,

which lacks the canonical septal PG concentric-ring architecture, is exploited in high-level MRSA, where *rpoB** in combination with *mecA* allows division in the presence of antibiotics.

Dual mechanisms for high-level MRSA

High-level MRSA requires two factors; the presence of PBP2a and a potentiator (*pot*) mutation (as provided by *rpoB**) (13, 14). For high-level MRSA to grow and divide in the presence of β -lactam antibiotics, the essentiality of PBP1 and PBP2 transpeptidase activities must be circumvented or enzymatically complemented. Previous studies report that in strain COL the transpeptidase activity of PBP2 can be complemented by the presence of PBP2a (21, 22). However, growth of a COL derivative lacking PBP2 protein is impaired and does not exhibit antibiotic resistance (22). This is because PBP2 transglycosylase activity is required to act cooperatively with PBP2a (22). COL also harbours potentiator *rpoB** mutations (A798V, S875L) required for high-level resistance (14). To determine whether there are two co-dependent mechanisms that in combination lead to high-level MRSA we investigated the effect of *pbp2* mutations. As expected from previous reports (21, 22) PBP2 is essential and PBP2a and/or *rpoB** (H929Q) could not compensate for the loss of PBP2 protein in terms of plating efficiency and growth (fig. S8A-C). When PBP2 was depleted, with or without the presence of PBP2a, *S. aureus* stopped dividing, exhibiting decreased septal PG incorporation and altered septal morphology (fig. S9). Loss of PBP2 also led to a decrease in cell size (fig. S9H). Depletion of PBP2 in *rpoB** or *mecA*⁺ *rpoB** led to lower growth, decreased septal PG incorporation, altered septal morphology, and death (fig. S9C, D, and G). We could not create PBP2* (transpeptidase mutant) strains in either the parental SH1000 or *rpoB** backgrounds, indicating its essentiality. However, strains where only PBP2* is present were viable in both *mecA*⁺ and *mecA*⁺ *rpoB** (Fig. 3A to D). Both the PBP2 and PBP2* constructs were verified by Western blot and Bocillin labelling (fig. S8D and E). Both strains with PBP2* were able to grow with near parental (*mecA*⁺ and *mecA*⁺ *rpoB**, respectively) cell morphology (fig. S9E and F). All PBP2 and PBP2* constructs demonstrate a diminished cell size compared to SH1000 (fig. S9H). Expression of PBP2* (lacking PBP2 transpeptidase activity) in the *mecA*⁺ or *mecA*⁺ *rpoB** backgrounds resulted in septa that exhibited the typical PG concentric-ring architecture, with strands preferentially oriented in the circumferential direction (Fig. 3E and F and fig. S10). We conclude that neither PBP2 nor PBP2a are responsible, even in part, for the PG septal concentric rings associated with conventional cell division. Therefore, there are two factors required for high-level MRSA: (i) PBP2a replaces the essential transpeptidase activity of PBP2, and (ii) a *pot* mutation (e.g. *rpoB**) permits cell division without PBP1 transpeptidase activity.

Potentiator mutations converge on nucleotide signalling

Mutations in *rpoB* and *rpoC* have been associated with clinically important high-level MRSA strains and the conversion from hetero- to homogeneous resistance (13, 14, 23, 24). Other *pot* mutations, such as *rel*, *clpXP*, *gdpP*, *pde2* and *lytH* have been uncovered in laboratory studies and in some cases clinically (13). Whilst other mutations enhanced the MIC of *mecA*⁺, tested in our defined SH1000 background with a single copy of *mecA* in the chromosome, only *rpoB* and *rel* led to high-level resistance (table S1; MIC ≥ 256 $\mu\text{g ml}^{-1}$).

The *rel* gene encodes a key component of the stringent response (25) and whilst the gene is conditionally essential, the *pot* mutant strain (*rel**) has a C-terminal truncation in the regulatory domain of the Rel protein, and likely increases (p)ppGpp levels (26). The stringent response has been previously implicated as having a major role in potentiating high-level MRSA (27) and here we found the presence of *mecA*⁺ *rpoB** led to a significant increase in the levels of the stringent response signalling molecules ppGpp and pppGpp (Fig. 4A). To determine the

relationship between the stringent response and the dual pathways to high-level MRSA we investigated its ability to compensate for the loss of PBP1 transpeptidase activity (Fig. 4B). The *rel** mutation was as effective as *rpoB** in compensating for the absence of PBP1 transpeptidase activity as judged by measurement of plating efficiency (Fig. 4B), implicating the stringent response in the ability to grow and divide without septal PG concentric rings.

Therapeutic development for MRSA

To counter the emergence of MRSA, compounds have been identified that resensitize these strains to β -lactams (28). These include clomiphene (29) and norgestimate (30), as well as natural products including epicatechin gallate (ECg) (31) and spermine (32). Their mode of action is mostly unknown and so we tested their effect, at concentrations that resensitize *mecA*⁺ *rpoB** and the other clinical MRSA strains to oxacillin but do not inhibit growth without antibiotic (see Materials and Methods) (Fig. 4C to E). Clomiphene and spermine did not inhibit the plating efficiency of *pbp1** *rpoB** but did for both *mecA*⁺ *pbp2** and *mecA*⁺ *pbp2** *rpoB**, suggesting a link to the activity of PBP2a. Norgestimate impaired the plating efficiency of *pbp1** *rpoB** and *mecA*⁺ *pbp2** but not *mecA*⁺ *pbp2** *rpoB**, demonstrating a potential cross-talk between the co-dependent pathways (i.e., acquisition of *mecA* and a *pot* mutation) that lead to resistance. ECg inhibited the plating efficiency of all three strains indicating that it may affect an Aux factor required under all conditions. These observations further differentiate the two resistance pathways and provide specific interventions able to dissect the new mode of cell division uncovered here.

Discussion

We have revealed that the high-level resistance to β -lactam antibiotics exhibited by some MRSA strains is linked to an alternative mode of cell division set within the context of wider physiological adaptations (i.e., increased ppGpp and pppGpp) (Fig. 4F). The development of high-level MRSA is a two-step process in which PBP2a compensates for the lack of native PBP2 transpeptidase activity in the presence of β -lactam antibiotics (22). PBP2 is an essential enzyme that is required for the synthesis of the dense mesh PG on the inside of the cell wall at both the septum and the cell periphery. It is therefore the major PBP in terms of bulk PG synthesis. PBP2a cannot compensate for the lack of PBP2 protein (specifically its transglycosylase activity (22)). However, as PBPs can form dimers (33), PBP2/2a heterodimers could allow both the multiple protein interactions of PBP2 (34) and PBP2a transpeptidase activity required for PG synthesis. PBP1 has essential transpeptidase activity and operates with its cognate transglycosylase FtsW (35). Here we show that PBP1 activity is responsible for the formation of the concentric rings that are characteristic of septal PG. PBP2a cannot compensate for the lack of PBP1 activity but *pot* mutations can. The *pot* mutations permit successful cell division without septal PG rings in the presence of high levels of antibiotics (Fig. 4F). This compensatory mechanism does not involve a replacement of PBP1 activity but rather physiological adaptations that allow division without it. A question arises as to whether the ability to divide without septal PG concentric rings in high-level MRSA strains evolved specifically, in the context of antibiotic use, or whether it is part of a wider physiological capability that is deployed under stressful conditions? Mutations in *rpo* genes are often found associated with antibiotic and stress resistance in *S. aureus* and many other organisms (24, 36, 37). A survey of 1,429 MRSA (ST22) clinical strains revealed that ~10% had at least one point mutation in genes coding for core RNAP subunits or σ factors (24). The current study now links these mutations to the widely conserved stringent response, which is a key component in bacterial responses to stress and growth perturbations (25). Our *rpoB** strains exhibit lower

278 growth rates compared to parental strains (14), which could, at least in-part, facilitate the
279 alternative mode of division.

280 Given the array of MRSA SCC_{mec} types and clonal lineages, it is likely that the effects of *pot*
281 factors, such as *rpo**, are influenced by the genetic background (13). This provides both
282 complexity in unravelling the interplay between *pot* and *aux* factors but also an opportunity to
283 establish those common, underlying principles that underpin resistance. The resensitizing
284 agents also provide avenues to probe underlying molecular mechanisms. Our study has
285 revealed insights into antibiotic resistance and facets of cell division in *S. aureus*. It is by
286 studying these processes in tandem that we can understand basic mechanisms of the bacterial
287 cell cycle and reveal ways to control antibiotic resistance.

References

1. B. Ribeiro da Cunha, L. P. Fonseca, C. R. C. Calado, Antibiotic discovery: Where have we come from, where do we go? *Antibiot.* **8**, 1-21 (2019).
2. Antimicrobial Resistance Collaborators, Global burden of bacterial antimicrobial resistance in 2019: a systematic analysis. *Lancet* **399**, 629–655 (2022).
3. S. Lakhundi, K. Zhang, Methicillin-resistant *Staphylococcus aureus*: Molecular characterization, evolution, and epidemiology. *Clin. Microbiol. Rev.* **31**:10.1128/cmr.00020-18 (2018).
4. B. J. Hartman, A. Tomasz, Low-affinity penicillin-binding protein associated with beta-lactam resistance in *Staphylococcus aureus*. *J. Bacteriol.* **158**, 513–516 (1984).
5. W. Vollmer, D. Blanot, M. A. De Pedro, Peptidoglycan structure and architecture. *FEMS Microbiology Reviews* **32**, 149–167 (2008).
6. L. Pasquina-Lemonche, J. Burns, R. D. Turner, S. Kumar, R. Tank, N. Mullin, J. S. Wilson, B. Chakrabarti, P. A. Bullough, S. J. Foster, J. K. Hobbs, The architecture of the Gram-positive bacterial cell wall. *Nature* **582**, 294–297 (2020).
7. S. F. Pereira, A. O. Henriques, M. G. Pinho, H. de Lencastre, A. Tomasz, Role of PBP1 in cell division of *Staphylococcus aureus*. *J. Bacteriol.* **189**, 3525–3531 (2007).
8. K. Wacnik, V. A. Rao, X. Chen, L. Lafage, M. Pazos, S. Booth, W. Vollmer, J. K. Hobbs, R. J. Lewis, S. J. Foster, Penicillin-Binding Protein 1 (PBP1) of *Staphylococcus aureus* has multiple essential functions in cell division. *mBio*. **13**, e00669 (2022).
9. M. G. Pinho, S. R. Filipe, H. de Lencastre, A. Tomasz, Complementation of the essential peptidoglycan transpeptidase function of penicillin-binding protein 2 (PBP2) by the drug resistance protein PBP2A in *Staphylococcus aureus*. *J. Bacteriol.* **183**, 6525–6531 (2001).
10. E. García-Fernández, G. Koch, R. M. Wagner, A. Fekete, S. T. Stengel, J. Schneider, B. Mielich-Süss, S. Geibel, S. M. Markert, C. Stigloher, D. Lopez, Membrane microdomain disassembly inhibits MRSA antibiotic resistance. *Cell* **171**, 1354-1367.e20 (2017).
11. L. H. Otero, A. Rojas-Altuve, L. I. Llarrull, C. Carrasco-López, M. Kumarasiri, E. Lastochkin, J. Fishovitz, M. Dawley, D. Hsek, M. Lee, J. W. Johnson, J. F. Fisher, M. Chang, S. Mobashery, J. A. Hermoso, How allosteric control of *Staphylococcus aureus* penicillin binding protein 2a enables methicillin resistance and physiological function. *PNAS* **110**, 16808-16813 (2013).
12. B. J. Hartman and, A. Tomasz, Expression of methicillin resistance in heterogeneous strains of *Staphylococcus aureus*. *Antimicrob. Agents Chemother.* **29**, 85–92 (1986).
13. B. L. Bilyk, V. V. Panchal, M. Tinajero-Trejo, J. K. Hobbs, S. J. Foster, An Interplay of multiple positive and negative factors governs methicillin resistance in *Staphylococcus aureus*. *Microbiol. Mol. Biol. Rev.* **86**, e00159 (2022).
14. V. V. Panchal, C. Griffiths, H. Mosaei, B. Bilyk, J. A. F. Sutton, O. T. Carnell, D. P. Hornby, J. Green, J. K. Hobbs, W. L. Kelley, N. Zenkin, S. J. Foster, Evolving MRSA: High-level β -lactam resistance in *Staphylococcus aureus* is associated with RNA Polymerase alterations and fine tuning of gene expression. *PLOS Pathog.* **16**, e1008672 (2020).
15. B. Salamaga, L. Kong, L. Pasquina-Lemonche, L. Lafage, M. von Und Zur Muhlen, J. F. Gibson, D. Grybchuk, A. K. Tooke, V. Panchal, E. J. Culp, E. Tatham, M. E. O’Kane, T. E. Catley, S. A. Renshaw, G. D. Wright, P. Plevka, P. A. Bullough, A. Han, J. K. Hobbs, S. J. Foster, Demonstration of the role of cell wall homeostasis in *Staphylococcus aureus* growth and the action of bactericidal antibiotics. *PNAS* **118**, 1-8 (2021).

- 333 16. R. D. Turner, E. C. Ratcliffe, R. Wheeler, R. Golestanian, J. K. Hobbs, S. J. Foster,
334 Peptidoglycan architecture can specify division planes in *Staphylococcus aureus*. *Nat.*
335 *Commun.* **1**, 26 (2010).
- 336 17. S. R. Harris, E. J. Feil, M. T. G. Holden, M. A. Quail, E. K. Nickerson, N. Chantratita, S.
337 Gardete, A. Tavares, N. Day, J. A. Lindsay, J. D. Edgeworth, H. De Lencastre, J. Parkhill, S.
338 J. Peacock, S. D. Bentley, Evolution of MRSA during hospital transmission and
339 intercontinental spread. *Science* **327**, 469–474 (2010).
- 340 18. M. T. G. Holden, E. J. Feil, J. A. Lindsay, S. J. Peacock, N. P. J. Day, M. C. Enright, T. J.
341 Foster, C. E. Moore, L. Hurst, R. Atkin, A. Barron, N. Bason, S. D. Bentley, C. Chillingworth,
342 T. Chillingworth, C. Churcher, L. Clark, C. Corton, A. Cronin, J. Doggett, L. Dowd, T.
343 Feltwell, Z. Hance, B. Harris, H. Hauser, S. Holroyd, K. Jagels, K. D. James, N. Lennard, A.
344 Line, R. Mayes, S. Moule, K. Mungall, D. Ormond, M. A. Quail, E. Rabinowitsch, K.
345 Rutherford, M. Sanders, S. Sharp, M. Simmonds, K. Stevens, S. Whitehead, B. G. Barrell, B.
346 G. Spratt, J. Parkhill, Complete genomes of two clinical *Staphylococcus aureus* strains:
347 Evidence for the evolution of virulence and drug resistance. *PNAS* **101**, 9786–9791 (2004).
- 348 19. T. Takano, W. C. Hung, M. Shibuya, W. Higuchi, Y. Iwao, A. Nishiyama, I. Reva, O. E.
349 Khokhlova, S. Yabe, K. Ozaki, M. Takano, T. Yamamoto, A new local variant (ST764) of the
350 globally disseminated ST5 lineage of hospital-associated methicillin-resistant *Staphylococcus*
351 *aureus* (MRSA) carrying the virulence determinants of community-associated MRSA.
352 *Antimicrob. Agents Chemother.* **57**, 1589–1595 (2013).
- 353 20. B. A. Diep, S. R. Gill, R. F. Chang, T. H. Van Phan, J. H. Chen, M. G. Davidson, F. Lin, J. Lin,
354 H. A. Carleton, E. F. Mongodin, G. F. Sensabaugh, F. Perdreau-Remington, Complete genome
355 sequence of USA300, an epidemic clone of community-acquired methicillin-resistant
356 *Staphylococcus aureus*. *Lancet* **367**, 731–739 (2006).
- 357 21. M. G. Pinho, S. R. Filipe, H. De Lencastre, A. Tomasz, Complementation of the essential
358 peptidoglycan transpeptidase function of penicillin-binding protein 2 (PBP2) by the drug
359 resistance protein PBP2A in *Staphylococcus aureus*. *J. Bacteriol.* **183**, 6525–6531 (2001).
- 360 22. M. G. Pinho, H. de Lencastre, A. Tomasz, An acquired and a native penicillin-binding protein
361 cooperate in building the cell wall of drug-resistant staphylococci. *PNAS* **98**, 10886–10891
362 (2001).
- 363 23. Y. Aiba, Y. Katayama, T. Hishinuma, H. Murakami-Kuroda, L. Cui, K. Hiramatsu, Mutation
364 of RNA polymerase β -subunit gene promotes heterogeneous-to-homogeneous conversion of β -
365 lactam resistance in methicillin-resistant *Staphylococcus aureus*. *Antimicrob. Agents*
366 *Chemother.* **57**, 4861–4871 (2013).
- 367 24. A. Krishna, B. Liu, S. J. Peacock, S. Wigneshweraraj, The prevalence and implications of single
368 nucleotide polymorphisms in genes encoding the RNA polymerase of clinical isolates of
369 *Staphylococcus aureus*. *MicrobiologyOpen* **9**, e1058 (2020).
- 370 25. S. E. Irving, N. R. Choudhury, R. M. Corrigan, The stringent response and physiological roles
371 of (pp)pGpp in bacteria. *Nat. Rev. Microbiol.* **19**, 256–271 (2021).
- 372 26. A. T. Deventer, D. Bryson, M. Shortill, A. B. Boraston, J. K. Hobbs, Molecular characterization
373 of clinical rel mutations and consequences for resistance expression and fitness in
374 *Staphylococcus aureus*. *Antimicrob. Agents Chemother.* **66**, e00938 (2022).
- 375 27. C. Kim, M. Mwangi, M. Chung, C. Milheirico, H. de Lencastre, A. Tomasz, The mechanism
376 of heterogeneous beta-lactam resistance in MRSA: key role of the stringent stress response.
377 *PLoS One* **8**, e82814 (2013).
- 378 28. T. J. Foster, Can beta-Lactam antibiotics be resurrected to combat MRSA? *Trends Microbiol.*
379 **27**, 26–38 (2019).

380 29. M. A. Farha, T. L. Czarny, C. L. Myers, L. J. Worrall, S. French, D. G. Conrady, Y. Wang, E.
381 Oldfield, N. C. Strynadka, E. D. Brown, Antagonism screen for inhibitors of bacterial cell wall
382 biogenesis uncovers an inhibitor of undecaprenyl diphosphate synthase. *PNAS* **112**, 11048–
383 11053 (2015).

384 30. Y. Yoshii, K. I. Okuda, S. Yamada, M. Nagakura, S. Sugimoto, T. Nagano, T. Okabe, H.
385 Kojima, T. Iwamoto, K. Kuwano, Y. Mizunoe, Norgestimate inhibits staphylococcal biofilm
386 formation and resensitizes methicillin-resistant *Staphylococcus aureus* to β -lactam antibiotics.
387 *npj Biofilms Microbiomes* **3**, 18 (2017).

388 31. P. D. Stapleton, S. Shah, K. Ehler, Y. Hara, P. W. Taylor, The β -lactam-resistance modifier
389 (–)-epicatechin gallate alters the architecture of the cell wall of *Staphylococcus aureus*.
390 *Microbiology* **153**, 2093–2103 (2007).

391 32. D. H. Kwon, C. D. Lu, Polyamine effects on antibiotic susceptibility in bacteria. *Antimicrob.*
392 *Agents Chemother.* **51**, 2070–2077 (2007).

393 33. J. F. Fisher, S. Mobashery, β -Lactams against the Fortress of the Gram-Positive *Staphylococcus*
394 *aureus* Bacterium. *Chem. Rev.* **121**, 3412–3463 (2021).

395 34. V. R. Steele, A. L. Bottomley, J. Garcia-Lara, J. Kasturiarachchi, S. J. Foster, Multiple essential
396 roles for EzrA in cell division of *Staphylococcus aureus*. *Mol. Microbiol.* **80**, 542–555 (2011).

397 35. N. T. Reichmann, A. C. Tavares, B. M. Saraiva, A. Jouselin, P. Reed, A. R. Pereira, J. M.
398 Monteiro, R. G. Sobral, M. S. VanNieuwenhze, F. Fernandes, M. G. Pinho, SEDS-bPBP pairs
399 direct lateral and septal peptidoglycan synthesis in *Staphylococcus aureus*. *Nat. Microbiol.* **4**,
400 1368–1377 (2019).

401 36. L. Ostrer, Y. Ji, A. Khodursky, Identification and characterization of pleiotropic high-
402 persistence mutations in the beta subunit of the bacterial RNA polymerase. *Antimicrob. Agents*
403 *Chemother.* **65**, 00522 (2021).

404 37. J. A. Leeds, M. Sachdeva, S. Mullin, S. W. Barnes, A. Ruzin, In vitro selection, via serial
405 passage, of *Clostridium difficile* mutants with reduced susceptibility to fidaxomicin or
406 vancomycin. *J. Antimicrob. Chemother.* **69**, 41–44 (2014).

407 38. <https://doi.org/10.15131/shef.data.26341735>

408 39. R. M. Corrigan, L. Bowman, A. R. Willis, V. Kaever, A. Grundling, Cross-talk between two
409 nucleotide-signaling pathways in *Staphylococcus aureus*. *J. Biol. Chem.* **290**, 5826–5839
410 (2015).

411 40. R. P. Novick, S. I. Morse, In vivo transmission of drug resistance factors between strains of
412 *Staphylococcus aureus*. *J. Exp. Med.* **125**, 45–59 (1967).

413 41. S. Schenk, R. A. Laddaga, Improved method for electroporation of *Staphylococcus aureus*.
414 *FEMS Microbiol. Lett.* **94**, 133–138 (1992).

415 42. J. Schindelin, I. Arganda-Carreras, E. Frise, V. Kaynig, M. Longair, T. Pietzsch, S. Preibisch,
416 C. Rueden, S. Saalfeld, B. Schmid, J. Y. Tinevez, D. J. White, V. Hartenstein, K. Eliceiri, P.
417 Tomancak, A. Cardona, Fiji: an open-source platform for biological-image analysis. *Nat.*
418 *Methods* **9**, 676–682 (2012).

419 43. J. G. Beton, R. Moorehead, L. Helfmann, R. Gray, B. W. Hoogenboom, A. P. Joseph, M. Topf,
420 A. L. B. Pyne, TopoStats - A program for automated tracing of biomolecules from AFM
421 images. *Methods* **193**, 68–79 (2021).

422 44. T. Lindeberg, Edge Detection and Ridge Detection with Automatic Scale Selection. *Int. J.*
423 *Comput. Vis.* **30**, 117–156 (1998).

424 45. F. Meyer, Topographic distance and watershed lines. *Signal Processing* **38**, 113–125 (1994).

- 425 46. <https://doi.org/10.5281/zenodo.13082796>
- 426 47. <https://doi.org/10.5281/zenodo.13133978>
- 427 48. S. Berg, D. Kutra, T. Kroeger, C. N. Strachle, B. X. Kausler, C. Haubold, M. Schiegg, J. Ales,
428 T. Beier, M. Rudy, K. Eren, J. I. Cervantes, B. Xu, F. Beuttenmueller, A. Wolny, C. Zhang, U.
429 Koethe, F. A. Hamprecht, A. Kreshuk, ilastik: interactive machine learning for (bio)image
430 analysis. *Nat. Methods* **16**, 1226–1232 (2019).
- 431 49. <https://doi.org/10.5281/zenodo.13134076>
- 432 50. M. J. Horsburgh, J. L. Aish, I. J. White, L. Shaw, J. K. Lithgow, S. J. Foster, δ b modulates
433 virulence determinant expression and stress resistance: Characterization of a functional rsbU
434 strain derived from *Staphylococcus aureus* 8325-4. *J. Bacteriol.* **184**, 5457–5467 (2002).
- 435 51. W. M. Shafer, J. J. Landolo, Genetics of staphylococcal enterotoxin B in methicillin-resistant
436 isolates of *Staphylococcus aureus*. *Infect. Immun.* **25**, 902–911 (1979).
- 437 52. B. N. Kreiswirth, S. Löfdahl, M. J. Betley, M. O'reilly, P. M. Schlievert, M. S. Bergdoll, R. P.
438 Novick, The toxic shock syndrome exotoxin structural gene is not detectably transmitted by a
439 prophage. *Nature* **305**, 709–712 (1983).
- 440 53. C. Y. Lee, S. L. Buranen, Y. Zhi-Hai, Construction of single-copy integration vectors for
441 *Staphylococcus aureus*. *Gene* **103**, 101–105 (1991).
- 442 54. G. McVicker, T. K. Prajsnar, A. Williams, N. L. Wagner, M. Boots, S. A. Renshaw, S. J. Foster,
443 Clonal expansion during *Staphylococcus aureus* infection dynamics reveals the effect of
444 antibiotic intervention. *PLoS Pathog.* **10**, e1003959 (2014).
- 445 55. P. D. Fey, J. L. Endres, V. K. Yajjala, T. J. Widhelm, R. J. Boissy, J. L. Bose, K. W. Bayles, A
446 genetic resource for rapid and comprehensive phenotype screening of nonessential
447 *Staphylococcus aureus* genes. *mBio.* **4**, 00537 (2013).
- 448 56. R. M. Corrigan, J. C. Abbott, H. Burhenne, V. Kaefer, A. Grundling, c-di-AMP is a new second
449 messenger in *Staphylococcus aureus* with a role in controlling cell size and envelope stress.
450 *PLoS Pathog.* **7**, e1002217 (2011).
- 451 57. V. A. Lund, K. Wacnik, R. D. Turner, B. E. Cotterell, C. G. Walther, S. J. Fenn, F. Grein, A. J.
452 M. Wollman, M. C. Leake, N. Olivier, A. Cadby, S. Mesnage, S. Jones, S. J. Foster, Molecular
453 coordination of *Staphylococcus aureus* cell division. *eLife* **7**, e32057 (2018).
- 454 58. M. Arnaud, A. Chastanet, M. Débarbouillé, New vector for efficient allelic replacement in
455 naturally nontransformable, low-GC-content, gram-positive bacteria. *Appl. Environ.*
456 *Microbiol.* **70**, 6887–6891 (2004).

457 Acknowledgements

458 We are grateful to Nicholas Mullin, Xinyue Chen, Anaam Alomari, Viralkumar V. Panchal,
459 Bartek Salamaga, and Matthew J. Barker for helpful discussions, also Jodi Lindsay (St.
460 George's UCL) and James O'Gara (University of Galway) for provision of strains. Electron
461 Microscopy was carried out at the School of Biosciences Cryo-Electron Microscopy Facility,
462 University of Sheffield. Fluorescence microscopy was performed at the Wolfson Light
463 Microscopy Facility, University of Sheffield. The research was in part carried out at the
464 National Institute for Health and Care Research (NIHR) Sheffield Biomedical Research Centre
465 (BRC). For the purpose of open access, the authors have applied a CC BY public copyright
466 license to any author accepted manuscript version arising from this submission. **Funding:** This
467 work was supported by the Engineering and Physical Sciences Research Council (grant
468 EP/T002778/1 to J.K.H. and S.J.F), the Wellcome Trust (grants 212197/Z/19/Z to J.K.H and
469 S.J.F and 104110/Z/14/A to J.K.H., S.J.F., J.G. and R.M.C) and the Biotechnology and

Biological Sciences Research Council (grant BB/R018383/1 to WMD). **Author contributions:** A.F.A.-O, and K.W designed the study, performed experiments, analysed, and interpreted data, and wrote the manuscript. (A.F.A.-O.: Figs. 1, 2, 3, Supplementary Materials Figs. S1-S3, S6 & S10; K.W.: Figs. 2-4, Supplementary Materials Figs. S4-S9). L.L., M.T.-T., B.B., S.E.I., J.A.F.S and C.J.P.-R. performed the experiments, analysed, and interpreted the data (L.L. Fig. 1, Supplementary Materials: Figs. S4 & S6; M.T.-T.: Fig. 4, Supplementary Materials Figs. S4, S8, S10; S.E.I.: Fig. 4; J.A.F.S.: Supplementary Materials: Fig. S3 & Table S1 and C.J.P.-R.: Supplementary Materials Fig. S10). L.P.-L. and D.S.O. developed the semi-automated macro used to calculate cell volume measurements and L.P.-L analysed the data (Supplementary Materials Figs. S4, S5 & S9). Also, L.P.-L. developed the semi-automated macro used to calculate the cell wall pore area (Supplementary Materials Figs. S2, S6, S10). S.A.R and E.B. performed the experiments and analyzed data (Supplementary Materials Fig. S2). O.M. and W.M.D. developed Matlab-based software used for the fibre detection (Figs. 1-3). D.J.H., J.F., R.C. and J.G. analysed and interpreted data, and wrote and reviewed the manuscript. J.K.H. and S.J.F. designed the study, interpreted the data, wrote the manuscript and directed the project. **Competing interests:** The authors declare no competing interests. **Data and materials availability:** The data that support the findings of this study are available in the Online Research Data (ORDA) figshare from the University of Sheffield with the identifier (38).

Supplementary Materials

Materials and Methods

Figs. S1 to S10

Tables S1 and S4

References (39 - 58)

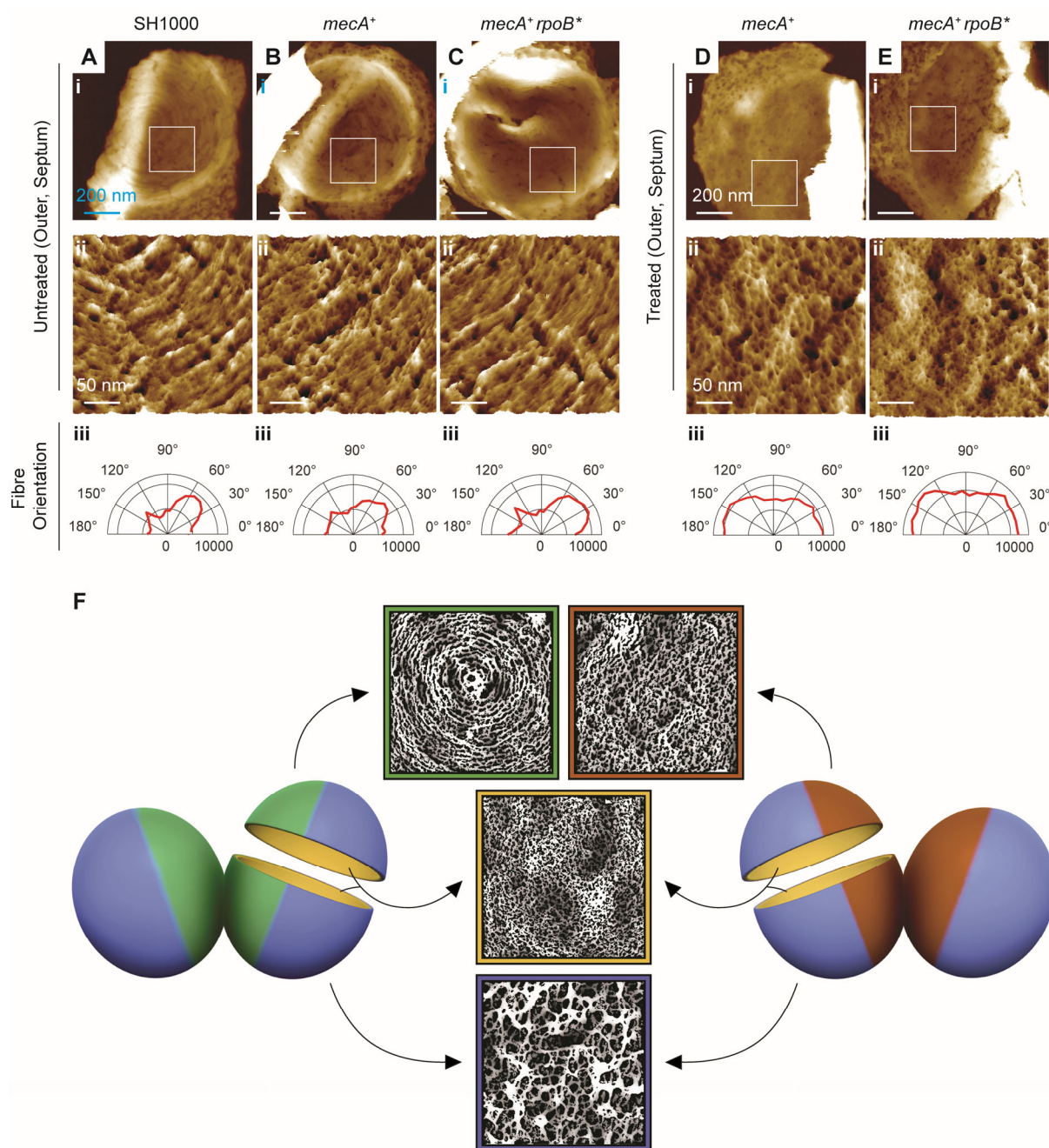


Fig. 1. Methicillin treatment of MRSA alters the architecture of the cell wall. From left to right, (A-C) show the outer surfaces of newly revealed septa, in samples of isolated sacculi of untreated (A) SH1000, (B) *mecA*⁺, and (C) *mecA*⁺ *rpoB*^{*} respectively. (D-E) Show the outer surface of the newly revealed septa of (D) *mecA*⁺ and (E) *mecA*⁺ *rpoB*^{*} treated with methicillin (1.5 and 25 $\mu\text{g ml}^{-1}$ respectively). In all columns: (i) shows an individual fragment of sacculus corresponding to the outer surface of the septum. Topographical height (z) range presented in each of these images (from left to right) is 140, 140, 150, 120, and 185 nm. (ii) Shows pseudo-three dimensional (3D) high resolution AFM images of the sections indicated by the white boxes in (i). Topographical height (z) range presented in each of these images (from left to right) is 7.5, 10, 7.5, 12, and 20 nm. (iii) Represents the combined angular histogram of fibre orientation of AFM high-resolution images similar to those in (ii). The fibre orientation analysis method used for the orientation detection is described in the Materials and Methods section. (F) Shows an interpretative diagram of different architectures (concentric rings, dense mesh, and open mesh) observed by high-resolution AFM on different surfaces (outer surface

509 of newly revealed septa, inner surface of the septa, and outer surface of cell periphery) of
510 untreated (left-hand side) and antibiotic treated (right-hand side) MRSA cell wall. The green
511 colour represents the concentric rings associated with the outer surface of the septum of
512 untreated cells, blue colour shows the open mesh at the cell periphery, yellow colour depicts
513 the dense mesh on the inner wall of the cell and lastly the brown colour represents the dense
514 mesh on the outer surface of the septum after treatment with methicillin. The modified AFM
515 images in Fig. 1F span 400 nm by 400 nm in x and y dimension.

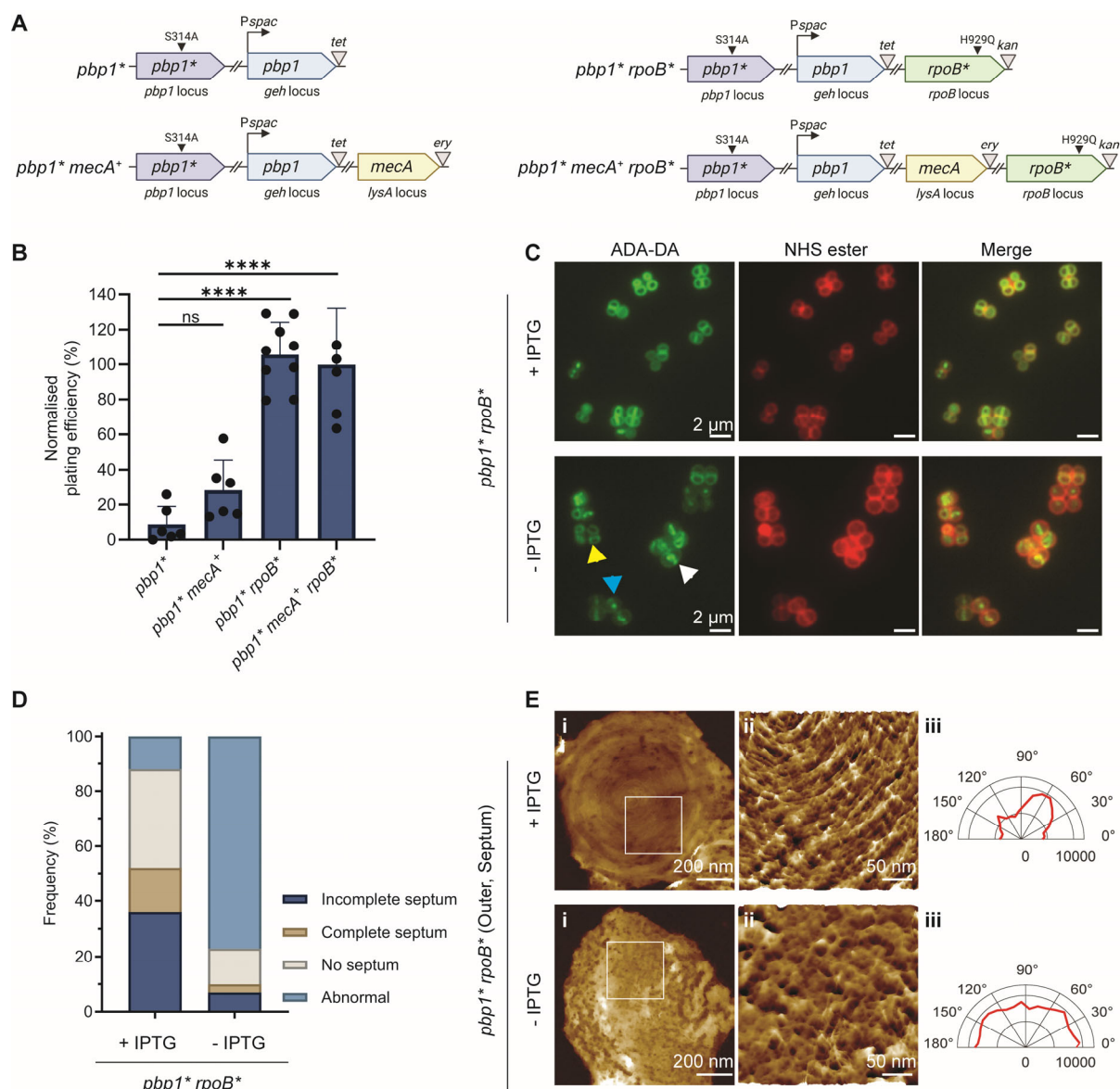


Fig. 2. Loss of PBP1 transpeptidase activity can be compensated for by *rpoB but not *mecA*.** (A) Representation of *pbp1** genetic constructs. An ectopic *pbp1* copy, at the lipase (*geh*) locus is controlled by the *Pspac* promoter. The *pbp1* gene at its native locus has a point mutation (940T>G) resulting in inactivation of transpeptidase activity (S314A, *pbp1**). The *mecA*⁺ gene is expressed from its native promoter at the *lysA* locus. In *rpoB**, a point mutation results in an amino acid substitution (H929Q) in RpoB. *tet*, *ery* and *kan* represent tetracycline, erythromycin and kanamycin resistance cassettes, respectively. The graphics were created with BioRender.com. (B) Plating efficiency of *pbp1**, *pbp1** *mecA*⁺, *pbp1** *rpoB** and *pbp1** *mecA*⁺ *rpoB** without IPTG. Plating efficiencies were compared to controls grown with IPTG, using a one-way ANOVA with Dunnett's multiple comparison test (ns, not significant; ****, *P* < 0.0001). Error bars show mean ± standard deviation (SD). (C) Fluorescence microscopy images of *pbp1** *rpoB** grown +/- IPTG for 4 h, labelled with ADA-DA (5 min) and then NHS-ester Alexa Fluor 555 to image nascent PG and cell wall, respectively. Images are z stack average intensity projections. Scale bars = 2 μm. (D) Quantification of cellular phenotypes based on ADA-DA incorporation in *pbp1** *rpoB** incubated with IPTG (+) or without IPTG (-), *n* = 511 and 654 (respectively). Examples of cells classified as abnormal with misshapen septal rings (yellow arrowhead), accumulation of ADA-DA at septal centre, 'plug' (blue arrowhead) and mislocalized ADA-DA incorporation (white arrowhead) are shown C. (E)

535 AFM images of newly exposed outer surface of the septum after cell division of *pbp1* rpoB**
536 grown +/- IPTG for 4 h, reveal lack of concentric-ring structures in -IPTG. (i) Representative
537 outer septal surfaces with height (z) range of 120 nm and the HS applies to both. (ii) Shows
538 pseudo-3D AFM high resolution images of the region within the white box in (i).
539 Topographical height (z) range (top) = 9.5 nm, and HS (bottom) = 21 nm. (iii) Represents the
540 combined angular histogram of fibre orientation of AFM high resolution images similar to
541 those in (ii).

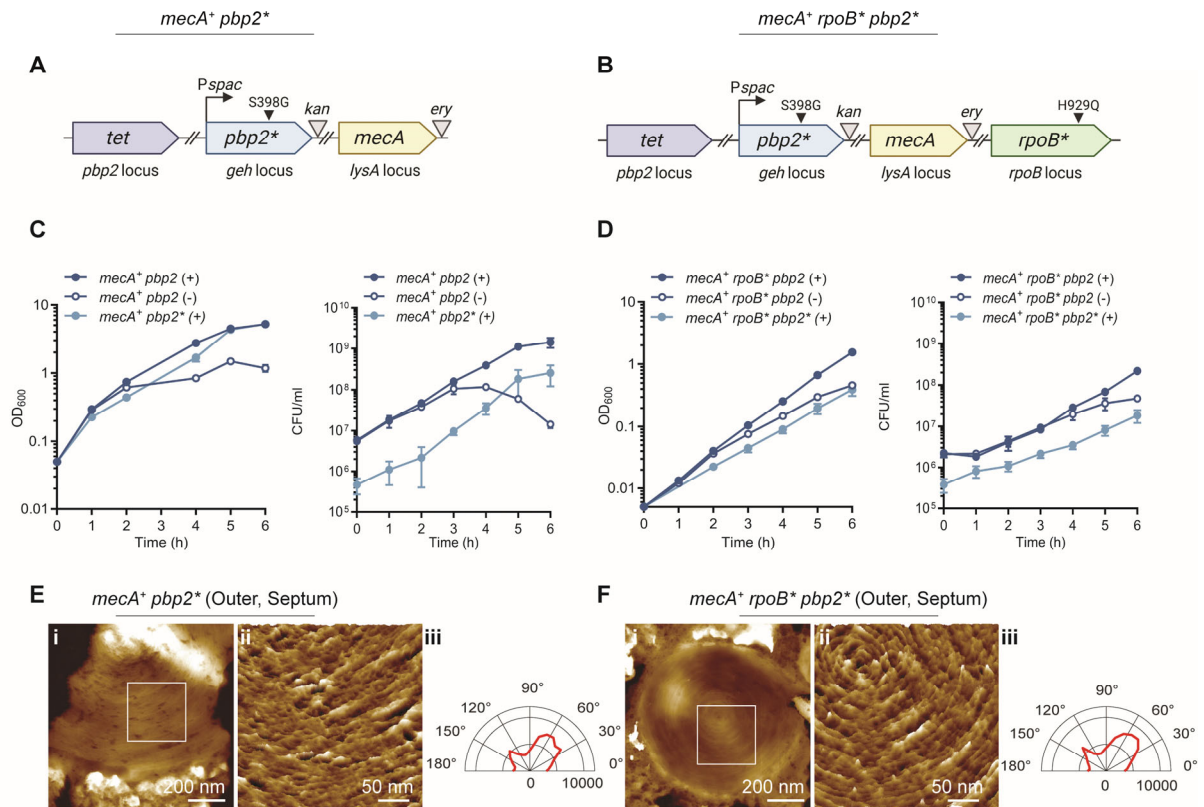


Fig. 3. Loss of PBP2 transpeptidase activity can be compensated for by *mecA* but not *rpoB*^{*}. (A-B) Schematic representation of *mecA*⁺ *pbp2*^{*} (SJF5807) and *mecA*⁺ *rpoB*^{*} *pbp2*^{*} (SJF5809) genetic constructs. A copy of *pbp2* with an inactive transpeptidase domain (*pbp2*^{*}, 1191-1192TC>GG, S398G) was placed under the control of the *Pspac* promoter at the lipase (*geh*) locus of SH1000, *pbp2* at its native locus was then deleted (marked with *tet*). In both strains, a copy of a *mecA* gene expressed from its native promoter was located at the *lysA* locus. In *mecA*⁺ *rpoB*^{*} *pbp2*^{*} (SJF5809) the *rpoB* gene has a point mutation which results in H929Q (*rpoB*^{*}). *ery* and *kan* represent erythromycin and kanamycin resistance cassettes, respectively. The graphics in (A-B) were created with BioRender.com. (C) Growth curves of *mecA*⁺ *pbp2*^{*} (SJF5663) grown in the presence (+) or absence (-) of IPTG, and *mecA*⁺ *pbp2*^{*} (SJF5807) (+ IPTG). (D) Growth curves of *mecA*⁺ *rpoB*^{*} *pbp2*^{*} (SJF5674) grown in the presence (+) or absence (-) of IPTG, and *mecA*⁺ *rpoB*^{*} *pbp2*^{*} (SJF5809) (+ IPTG). (E-F) AFM images of the newly revealed outer surface of septa after cell division of *mecA*⁺ *pbp2*^{*} (SJF5807) and *mecA*⁺ *rpoB*^{*} *pbp2*^{*} (SJF5809), respectively. In both E and F, (i) shows the outer surface of a representative septum. Topographical height (z) range of 130 nm applies to both. (ii) Shows a pseudo-3D high resolution image of the region within the white box in (i). Height range are 12 nm for E(ii) and 7 nm for F(ii). (iii) Represents the combined angular histogram of fibre orientation of AFM high resolution images similar to images in (ii).

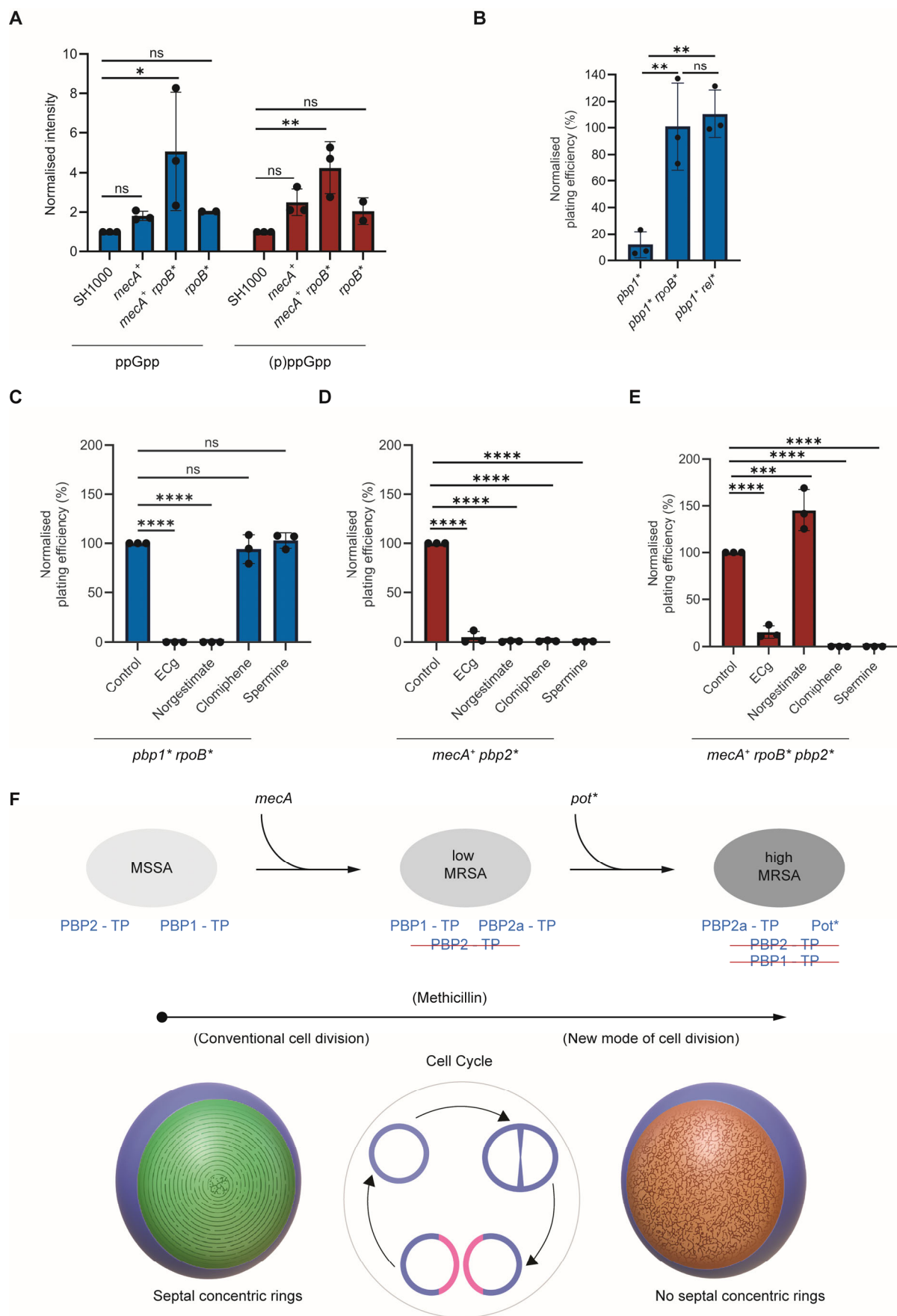


Fig. 4. Dual pathways to high-level MRSA. (A) Measurement of ppGpp and (p)ppGpp levels in SH1000, *mecA*⁺, *rpoB*^{*} and *mecA*⁺ *rpoB*^{*}, normalised to SH1000 and compared using one-

way ANOVA with Dunnet's multiple comparison test (ns, not significant; *, $P < 0.05$; **, $P < 0.01$). P values from left to right: 0.8727, 0.0425, 0.8290, 0.1470, 0.0051 and 0.4317. Error bars show the mean \pm SD. (B) Plating efficiency of *pbp1**, *pbp1** *rpoB** and *pbp1** *rel* without IPTG. Plating efficiency values were compared to controls with IPTG, using one-way ANOVA with Tukey's multiple comparison test (**, left to right $P = 0.0049$ and 0.003). Error bars show mean \pm SD. (C-E) Plating efficiency of (C) *pbp1** *rpoB**, (D) *mecA*⁺ *pbp2** and (E) *mecA*⁺ *rpoB** *pbp2** without IPTG supplemented with ECg, norgestimate, clomiphene or spermine. Data were compared to no inhibitor plates (Control) using a one-way ANOVA with Dunnett's multiple comparison test (ns, not significant; ****, $P < 0.0001$; ***, $P = 0.0004$). Error bars show mean \pm SD from three independent biological repeats. (F) Model for high-level MRSA development via acquisition of *mecA* and *pot* mutations (including *rpo** and *rel**), resulting in low-level (low) and subsequently high-level (high) resistance. In MSSA, without methicillin, PBP1 and PBP2 transpeptidases are active. In low-level MRSA, at intermediate methicillin levels sufficient to kill MSSA, PBP2 transpeptidase is inhibited but complemented by PBP2a. In high-level MRSA, at methicillin levels sufficient to kill MSSA and low-level MRSA, PBP2 and PBP1 transpeptidases are inhibited but complemented by PBP2a transpeptidase and Pot*, respectively. PBP1 transpeptidase is responsible for the characteristic septal PG concentric rings, during conventional cell division (green regions on blue cell background). In high-level MRSA, in the presence of methicillin, septal PG concentric rings are replaced by mesh (brown regions on blue cell background), revealing a novel mode of cell division requiring both PBP2a and Pot*.



Supplementary Materials for

Two co-dependent routes lead to high-level MRSA

Abimbola Feyisara Adedeji-Olulana^{1†}, Katarzyna Wacnik^{2,3,†}, Lucia Lafage^{2,3}, Laia Pasquina-Lemonche^{1,3}, Mariana Tinajero-Trejo^{2,3}, Joshua A. F. Sutton^{2,3}, Bohdan Bilyk^{2,3}, Sophie E. Irving^{2,3}, Callum J. Portman Ross^{2,3}, Oliver J. Meacock¹, Sam A. Randerson¹, Ewan Beattie¹, David S. Owen², James Florence^{2,3}, William M. Durham¹, David J. Hornby^{2,3}, Rebecca M. Corrigan^{2,3}, Jeffrey Green^{2,3}, Jamie K. Hobbs^{1,*}, Simon J. Foster^{2,3,*}

Corresponding author. Email: jamie.hobbs@sheffield.ac.uk; s.foster@sheffield.ac.uk.

The PDF file includes:

Materials and Methods

Figs. S1 to S10

Tables S1 to S4

Materials and Methods

Bacterial growth conditions

The strains used in this study are listed in Table S2. *S. aureus* strains were grown in tryptic soy broth (TSB), except for (p)ppGpp experiments which used low phosphate chemically defined medium (39) (CDM), at 37°C with aeration. For solid, Tryptic Soy Agar media (TSA), 1.5% (w/v) agar was added. When necessary, growth media were supplemented with kanamycin (50 µg ml⁻¹), tetracycline (1 µg ml⁻¹), chloramphenicol (10 µg ml⁻¹), erythromycin (5 µg ml⁻¹), lincomycin (25 µg ml⁻¹), methicillin (0.25, 1.5, 2, 25 or 40 µg ml⁻¹), isopropyl β-D-thiogalactopyranoside (IPTG; 50 µM or 1 mM) or mupirocin (60 µg ml⁻¹). For *mecA*⁺ *pbp2*^{*} (SJF5807) and *mecA*⁺ *rpoB*^{*} *pbp2*^{*} (SJF5809), 1 mM IPTG was added to growth media at all times.

Construction of plasmids

Escherichia coli NEB5α was used for the construction of all plasmids. Correct plasmid sequences were confirmed by DNA sequencing (Sanger sequencing by Source BioScience). Plasmids and oligonucleotides used in this study are listed in Table S3 and Table S4, respectively.

pKB-*Pspac-pbp2*

A fragment containing the full-length *pbp2* gene and its ribosome-binding site (RBS) was PCR amplified (from SH1000) using pCQ11-*pbp2*-F/-R primers and cloned into *Asc*I and *Nhe*I cut pCQ11-FtsZ-SNAP by Gibson assembly, resulting in pCQ11-*pbp2*. Next, the fragment containing the *Pspac* promoter, RBS and *pbp2* was PCR amplified from *S. aureus* SH1000 genomic DNA using pKB-*Pspac-pbp1*-F and pKB-*pbp2*-R and cloned into *Bam*HI and *Eco*RI cut pGM074, giving pKB-*Pspac-pbp2*.

pKB-*Pspac-pbp2*^{*}

A point mutation resulting in PBP2-TP inactivation (S398G) was introduced by site-directed mutagenesis using *pbp2*TP-F/-R primers and Q5 Site Directed Mutagenesis kit (New England Biolabs), creating pKB-*Pspac-pbp2*^{*}.

pMAD-Δ*pbp2*

One kb fragments upstream (up) and downstream (down) of *pbp2* were PCR amplified from *S. aureus* SH1000 genomic DNA using pMAD-Δ*pbp2*-F and *pbp2*-up-R, and *pbp2*-down-F and pMAD-Δ*pbp2*-R, respectively, while the tetracycline cassette (*tet*) was PCR amplified from pAISH1 using *tetR-pbp2*-F/-R primers. The up, *tet* and down fragments were ligated into *Eco*RI and *Bam*HI cut pMAD by Gibson assembly, resulting in pMAD-Δ*pbp2*.

Construction of mutants

All plasmids were introduced into restrictive-deficient *S. aureus* RN4220 and moved to a final *S. aureus* SH1000 strain by phage Φ11 transduction (40, 41). Whole genome sequencing was provided by MicrobesNG.

57 *pbp1* rpoB** and Δ *pbp1 rpoB**

58 Strains containing *pbp1** (SJF4656, SH1000 *geh::Pspac-pbp1 pbp1::pbp1* lacI*) and Δ *pbp1*
59 (SJF5106, SH1000 *geh::Pspac-pbp1 Δ pbp1 lacI*) were transduced with a phage lysate from
60 SJF5046 (SH1000 *lysA::mecA rpoB^{H929Qkan}*), resulting in *pbp1* rpoB** and Δ *pbp1 rpoB**.

61 *pbp2*

62 The pKB-*Pspac-pbp2* plasmid was used to transform *S. aureus* CYL316. The chromosomal
63 fragment containing the plasmid integrated in the *geh* locus was moved by phage transduction
64 into SH1000, resulting in SH1000 *geh::Pspac-pbp2* (SJF4924). SJF4924 was then transformed
65 with pMAD- Δ *pbp2*. Chromosomal integration of the plasmid at 42°C and excision at 28°C led
66 to a marked deletion of *pbp2* (*pbp2::tet*). To provide a control of *Pspac-pbp2*, *lacI* was
67 introduced by transduction using a phage lysate of VF17 (SH1000 *lacI*), resulting in the *pbp2*
68 mutant (SJF5630, SH1000 *geh::Pspac-pbp2 pbp2::tet lacI*).

69 *mecA⁺ pbp2* and *mecA⁺ rpoB* pbp2*

70 *Pspac-pbp2* from SJF4924 was transduced into *mecA⁺* (SJF4996, SH1000 *lysA::mecA*) and
71 *mecA⁺ rpoB** (SJF5003, SH1000 *lysA::mecA rpoB^{H929Q}*). Next, *pbp2* was deleted by
72 transducing *pbp2::tet* from SJF5630. Finally, *lacI* from VF17 was added, creating *mecA⁺ pbp2*
73 (SJF5663, SH1000 *lysA::pmecA geh::Pspac-pbp2 pbp2::tet lacI*) and *mecA⁺ rpoB* pbp2*
74 (SJF5674, SH1000 *lysA::pmecA rpoB^{H929Q} geh::Pspac-pbp2 pbp2::tet lacI*).

75 *rpoB* pbp2*

76 In the *rpoB** mutant (SJF5010, SH1000 *lysA::kan rpoB^{H929Q}*), the kanamycin resistance
77 cassette in the *lysA* locus was swapped for the erythromycin resistance cassette by phage
78 transduction of *lysA::ery* from GMSA015 (SH1000 *lysA::ery*). Next, *Pspac-pbp2* from
79 SJF4924, *pbp2::tet* from SJF5630 and *lacI* from VF17 were added, resulting in *rpoB* pbp2*
80 (SJF5690, SH1000 *lysA::ery rpoB^{H929Q} geh::Pspac-pbp2 pbp2::tet*).

81 *mecA⁺ pbp2** and *mecA⁺ rpoB* pbp2*

82 *S. aureus* CYL316 was transformed with pKB-*Pspac-pbp2**. The chromosomal fragment
83 carrying the integrated plasmid (*geh::Pspac-pbp2**) was transduced into *mecA⁺* (SJF4996) and
84 *mecA⁺ rpoB** (SJF5003). Next, *pbp2* was deleted by transducing *pbp2::tet* from SJF5630.
85 Finally, *lacI* from VF17 was added, giving *mecA⁺ pbp2** (SJF5807, SH1000 *lysA::pmecA*
86 *geh::Pspac-pbp2* pbp2::tet lacI*) and (SJF5809, SH1000 *lysA::pmecA rpoB^{H929Q} geh::Pspac-*
87 *pbp2* pbp2::tet lacI*).

88 *gdpP*, *lytH*, *pde2*, *clpP*, *clpX* and *rel*

89 SH1000 was transduced with a phage lysate from ANG1959 (SEJ1 *gdpP::kan*), NE1369 (JE2
90 *lytH::Tn*), NE1208 (JE2 *pde2::Tn*) or NE1714 (JE2 *rel::Tn*), resulting in *gdpP* (SJF5025,
91 SH1000 *gdpP::kan*), *lytH* (SJF5455, SH1000 *lytH::Tn*), *pde2* (SJF5454, SH1000 *pde2::Tn*),
92 *clpP* (SH1000 *clpP::Tn*), *clpX* (SH1000 *clpX::Tn*) and *rel* (SJF5457, SH1000 *rel::Tn*),
93 respectively.

94 *mecA⁺ gdpP*, *mecA⁺ lytH*, *mecA⁺ pde2*, *mecA⁺ clpP*, *mecA⁺ clpX* and *mecA⁺ rel*

95 The *mecA⁺* mutant (SJF4996, SH1000 *lysA::mecA*) was transduced with a phage lysate from
96 ANG195 (SEJ1 *gdpP::kan*), giving *mecA⁺ gdpP* (SJF5464, SH1000 *lysA::mecA gdpP::kan*).

97 SJF5324 (SH1000 *geh::mecA lysA::tet*) was transduced with a phage lysate from NE1369 (JE2
98 *lytH::Tn*), NE1208 (JE2 *pde2::Tn*) or NE1714 (JE2 *rel::Tn*), resulting in *mecA⁺ lytH* (SJF5461,
99 SH1000 *geh::mecA lysA::tet lytH::Tn*), *mecA⁺ pde2* (SJF5460, SH1000 *geh::mecA lysA::tet*
100 *pde2::TN*), *mecA⁺ clpP* (SH1000 *geh::mecA, clpP::Tn*), *mecA⁺ clpX* (SH1000 *geh::mecA,*
101 *clpX::Tn*) and *mecA⁺ rel* (SJF5463, SH1000 *geh::mecA lysA::tet rel::Tn*), respectively.

102 Directed evolution of high-level resistant MRSA strains

103 Using our previous approach (14), EMRSA15 and USA300 (minimal inhibitory concentration,
104 MIC 16-24 and 0.75 $\mu\text{g ml}^{-1}$, respectively) were plated on gradients of oxacillin (0-256
105 $\mu\text{g ml}^{-1}$) to select for high-level resistant derivatives. High level resistant clones (EMRSA15
106 (HL) and USA300 (HL), MIC >256 $\mu\text{g ml}^{-1}$ oxacillin for both) were picked and subjected to
107 whole genome sequencing. This revealed 3 single nucleotide polymorphisms (SNPs) for
108 USA300 (HL) (resulting in protein alterations LysS G429S, LysS R430H and
109 SAUSA300_0212 Q141*) and a total of 13 SNPs in 10 different genes for EMRSA15 (HL).

110 *pbp1* rel*

111 The *pbp1** mutant (SJF4656, SH1000 *geh::Pspac-pbp1 pbp1::pbp1* lacI*) was transduced
112 with a lysate from NE1714 (JE2 *rel::Tn*), giving *pbp1* rel* (SJF5513, SH1000 *geh::Pspac-*
113 *pbp1 pbp1::pbp1* lacI rel::Tn*).

114 Plating efficiency

115 Cells were grown from an OD₆₀₀ of 0.1 in TSB supplemented with 10 $\mu\text{g ml}^{-1}$ chloramphenicol
116 and 50 μM IPTG to early exponential phase (OD₆₀₀ ~0.3-0.5). Cells were then washed three
117 times in phosphate-buffered saline (PBS) and a dilution series of cell suspensions were plated
118 onto TSA containing 10 $\mu\text{g ml}^{-1}$ chloramphenicol, with or without 1 mM IPTG. For
119 experiments with sensitizing compounds, *pbp1* rpoB** (SJF5306) was grown as described
120 above and plated on TSA containing 10 $\mu\text{g ml}^{-1}$ chloramphenicol and a sensitizing compound.
121 *mecA⁺ pbp2** (SJF5807) and *mecA⁺ rpoB* pbp2** (SJF5809) were grown in TSB supplemented
122 with 10 $\mu\text{g ml}^{-1}$ chloramphenicol and 1 mM IPTG to exponential phase (OD₆₀₀ ~0.5) and plated
123 on TSA containing 10 $\mu\text{g ml}^{-1}$ chloramphenicol, 1 mM IPTG and a sensitizing
124 compound. Relative plating efficiency was expressed as the number of cells on plates without
125 IPTG, compared to the number of cells from plates with IPTG, multiplied by 100.

126 Depletion of PBP1 or PBP2

127 *Pspac-pbp1* and *Pspac-pbp2* containing strains were grown from an OD₆₀₀ of 0.1 to the
128 exponential phase (OD₆₀₀ ~0.3-0.5) in TSB supplemented with 10 $\mu\text{g ml}^{-1}$ chloramphenicol
129 and 50 μM IPTG. Cells were then washed three times by centrifugation and resuspension in
130 TSB and inoculated in fresh TSB containing 10 $\mu\text{g ml}^{-1}$ chloramphenicol to an OD₆₀₀ of 0.05
131 for phenotypic analysis, or to an OD₆₀₀ of 0.005 for growth studies. Control samples (+IPTG)
132 were grown in TSB supplemented with 10 $\mu\text{g ml}^{-1}$ chloramphenicol and 1 mM IPTG at all
133 times.

Growth in methicillin

High-level resistant, clinical MRSA strains and *mecA*⁺ *rpoB*^{*} (SJF5003) were grown overnight in the presence of 25 µg ml⁻¹ methicillin (or 50 µg ml⁻¹ where stated), diluted to an initial OD₆₀₀ of 0.05, prior to growth to exponential phase (OD₆₀₀ ~0.5) in the presence of 25 µg ml⁻¹ methicillin (or 50 µg ml⁻¹ where stated) at all times. This gives a total of over 8 generations in the presence of a high level of methicillin. This concentration of methicillin is sub-MIC for these strains and does not significantly affect growth rate in liquid culture. *mecA*⁺ (SJF4996) was grown in TSB overnight, diluted to an initial OD₆₀₀ of 0.05, prior to growth in the presence of 1.5 µg ml⁻¹ methicillin (sub-MIC) to exponential phase (OD₆₀₀ ~0.5). This concentration of methicillin is sub-MIC for this strain and does not significantly affect growth rate in liquid culture. Finally, SH1000 and *mecA*⁺ (SJF4996) were grown in TSB overnight, diluted to an initial OD₆₀₀ of 0.05, prior to growth to exponential phase (OD₆₀₀ ~0.5), followed by the addition of 1.5 µg ml⁻¹ methicillin (supra- and sub-MIC, respectively) and their phenotype followed over the next 3h.

MIC determination and evaluation of MRSA resensitizing compounds

Oxacillin MIC values were determined using E-test MIC Evaluator (Liofilchem or bioMérieux) strips in triplicate. MIC values of resensitizing compounds were determined for SH1000 by growth overnight in liquid TSB, for ECg (200 µg ml⁻¹), norgestimate (160 µg ml⁻¹), clomiphene (8 µg ml⁻¹) and spermine (320 µg ml⁻¹). Resensitization of *mecA*⁺ *rpoB*^{*} to oxacillin (from > 256 µg ml⁻¹ (control) to ≤ 4 µg ml⁻¹ (with resensitizer) was determined using ECg (50 µg ml⁻¹), norgestimate (10 µg ml⁻¹), clomiphene (4 µg ml⁻¹) or spermine (202 µg ml⁻¹) in TSA, spread with 200 µl of an overnight culture (diluted normalised to an OD₆₀₀ of ~2 in TSB) and overlaid with an E-test strip. The above resensitizer treatments also led to a drop in oxacillin MIC from > 256 µg ml⁻¹ to ≤ 12 µg ml⁻¹ for the clinical strains (COL, Mu50, MRSA252, TW20, USA300 (HL) and EMRSA15 (HL), apart for TW20 with norgestimate (170 µg ml⁻¹) and clomiphene (42 µg ml⁻¹). The effect of resensitizers on the growth of *S. aureus* strains was determined using the above sub-MIC concentration of compounds.

Fluorescence microscopy

Fixed and labelled cells were dried onto a poly-L-lysine-coated slide, mounted in SlowFade Gold (Thermo Fisher) and imaged using a Nikon Ti inverted microscope fitted with a Lumencor Spectra X light engine. Images were obtained using a 100× PlanApo (1.4 NA) oil objective using 1.518 RI oil and detected by an Andor Zyla sCMOS camera. The raw data in format .nd2 with three channels (ADA-DA, NHS-ester and brightfield) were used for cell volume and PG synthesis analysis.

PFA fixation

Cells were treated with 1.6% (wt/vol) paraformaldehyde for 30 min at RT and PFA removed by washing cells with water prior to imaging.

ADA-DA labelling

Cells were incubated with 1 mM ADA-DA (azido-D-alanyl-D-alanine, produced as previously described (8) at 37°C. Cells were washed, fixed with PFA, and labelled with Alexa Fluor 488 Alkyne (Merck) (for fluorescent labelling of the ADA-DA azide group) by the click reaction

175 (copper(I)-catalysed alkyne-azide cycloaddition) using the Click-iT™ Cell Reaction Buffer
176 Kit (Invitrogen) according to the manufacturer's instructions.

177 NHS-ester labelling

178 Cells were incubated with 8 µg ml⁻¹ NHS-ester Alexa Fluor 555 in PBS for 5 min on ice. Cells
179 were then washed in ice cold PBS and fixed with PFA.

180 Fluorescence intensity measurements

181 Fluorescence intensity of incorporated ADA-DA clicked to Atto488 was measured using Image
182 J/Fiji and calculated as counts/pixel.

183 Preparation of whole cell lysates

184 Cells resuspended in PBS were lysed using Lysing Matrix B and FastPrep homogeniser (MP
185 biomedical) in 10 cycles of 30 s, at speed of 6.5 m s⁻¹, with a 3-min incubation on ice between
186 cycles. Broken cells were separated from unbroken cells and lysing matrix by centrifugation
187 (5,000 x g, 5 min, 4°C). Total protein concentration was established using the BCA protein kit
188 (Pierce).

189 Western Blot

190 A total of 50 µg protein was separated on a 10% (w/v) SDS-PAGE gel and transferred onto a
191 nitrocellulose membrane. Membranes were blocked in 5% (w/v) skimmed-milk in TBST
192 (20 mM Tris-HCl, pH 7.6; 17 mM NaCl; 0.1% (v/v) Tween-20) and incubated with polyclonal
193 primary antibodies (1:1,000 dilution for anti-PBP1; 1:2,500 dilution for anti-PBP2) overnight
194 at 4°C. For detection, horseradish peroxidase-conjugated goat anti-rabbit IgG (Sigma; 1:10,000
195 dilution) and Clarity Western ECL Substrate (BioRad) were used according to the
196 manufacturer's instructions. Chemiluminescence was detected using Syngene G:BOX Chemi
197 XX9.

198

199 BocillinFL gel-based analysis

200 BocillinFL binding was adapted from a published method (35). Whole cell lysates (50 µg total
201 protein) were incubated with 100 µM BocillinFL (Invitrogen) for 15 min at 30°C. The reaction
202 was stopped by the addition of 5x SDS-PAGE loading buffer and incubation for 15 min at
203 30°C. The proteins were separated on a 10% (w/v) SDS-PAGE gel and visualized using a Bio-
204 Rad ChemiDoc MP imaging system or a GE Typhoon FLA 9500.

205 Transmission electron microscopy (TEM)

206 Cell preparation for electron microscopy was performed as described previously (15). Cell
207 pellets (5 ml cultures) were fixed overnight at 4°C in 2.5% (w/v) EM grade glutaraldehyde
208 (Agar Scientific). Samples were washed with PBS and resuspended in 2% (w/v) aqueous
209 osmium tetroxide (Agar Scientific) for secondary fixation (2 h at room temperature). Cells were
210 washed with PBS and dehydrated by incubating with increasing concentrations of ethanol (60,
211 75, 95 and 100% (v/v) ethanol) 15 min each. Ethanol was removed and samples were incubated
212 with propylene oxide (Agar Scientific) to complete dehydration. Samples were mixed with a

1:1 mix of propylene oxide and Epon resin (Agar Scientific) and incubated overnight at room temperature to allow infiltration. The majority of the resin was removed, and the excess of propylene oxide evaporated at room temperature. Two consecutive incubations of the samples with pure Epon resin (4 h each) were performed and cells were embedded in fresh resin. Resin polymerisation was achieved by incubation at 60°C for 48 h. Thin sections (85 nm) were produced using an Ultracut E Ultramicrotome (Reichert-Jung) and mounted onto 300-square mesh nickel TEM grids (Agar Scientific). Sections were stained in 3% (w/v) aqueous uranyl acetate (Polysciences Inc., 21447) for 25 min, washed with dH₂O and stained with Reynold's lead citrate for 5 min. The citrate was removed by washing with dH₂O. A FEI Tecnai T12 Spirit Transmission Electron Microscope operating at 80 kV was used for imaging. A Gatan Orius SC1000B bottom-mounted CCD camera recorded the images. EM images were analysed using Fiji (42). Over 300 cells were counted for each repeat, with at least two independent repeats per sample/treatment. Cells were categorised according to their phenotypic features as normal and abnormal, dependent on septal misplacement or growth defects.

Extraction and purification of PG

PG was extracted as previously described (16). Briefly, cells were grown in the presence or absence of IPTG for 2-4 h for PBP1 and PBP2 depletion experiments or to mid-exponential phase with or without methicillin for methicillin-treatment experiments and boiled at 100°C for 15 min to kill the cells. Boiled cells were recovered by centrifugation at 20,000 x g for 3 min and the supernatant was discarded. Next, the pellets were suspended in PBS and transferred to the lysing matrix tubes containing 0.1 mm silica beads and broken using FastPrep 24 Homogeniser (10 cycles of 30 s, at speed of 6.5 m s⁻¹, with a 3-min incubation on ice between cycles). Next, the tubes were centrifuged at 170 x g at RT to remove the beads and the supernatant, containing the broken cells, was pipetted into new Eppendorf tubes, which were then centrifuged at 20,000 x g at RT for 3 min. PG was resuspended in 5% (w/v) SDS solution and boiled at 100°C for 25 min. Boiling in SDS was repeated one more time for 15 min and the PG was serially rinsed with Milli-Q water. Lastly, PG was resuspended in a solution of 50 mM Tris HCl pH 7, containing 2 mg ml⁻¹ of pronase, and incubated at 60°C for 90 min. Afterwards, PG was rinsed thrice with HPLC grade water, and stored at 4°C without any further treatment.

PG immobilisation and AFM imaging

To immobilise purified PG, a mica substrate was coated with Cell-tak (Corning, Netherlands), which is a solution of polyphenolic proteins. Briefly, the mica substrate was incubated with 180 µl of Cell-tak solution (171 µl of 100 mM sodium bicarbonate (NaHCO₃) pH 8.0, 3 µl of 1 M sodium hydroxide (NaOH), and 6 µl of 1.05 mg ml⁻¹ Cell-tak) for 30 min. Next, the substrate was rinsed three times with HPLC grade water and then dried with nitrogen flow. Fifty microliters of diluted PG solution was then added to the Cell-tak coated substrate, incubated for 1 h and rinsed with HPLC grade water and dried with nitrogen flow. For thickness measurements, AFM height topographic images of dehydrated PG were captured in air using AFM tapping mode with Nunano SCOUT 350 - Silicon AFM probe (spring constant: 42 N/m, Resonance frequency: 350 kHz) at free amplitude of 10 nm with set point of 70-80% of free amplitude (e.g. 7 nm) on a Dimension FastScan Bio (Bruker, Santa Barbara). For AFM high-resolution imaging, all the high-resolution images were acquired in Peak force tapping mode in imaging buffer (10 mM Tris; 200 mM KCl; 10 mM MgCl₂, pH 8.0) with the Bruker Fastscan-D cantilevers at the range of 1-3 nN peak force set point on a Dimension FastScan AFM (Bruker, Santa Barbara). The imaging parameters used are as follows; Scan rate: 1 Hz; Scan angle: 0°; Peak Force frequency: 2-8 kHz, Peak force amplitude: 80-100 nm, and with

260 high pixel resolution. Prior to high-resolution imaging, the spring constant and deflection
261 sensitivity of the cantilevers were calculated using the Sader thermal spectra method.

262 PG thickness measurement data processing

263 To manually measure the thickness of AFM topographic height images of dehydrated PG were
264 imported into Gwyddion 2.55, masked and levelled using first order polynomial row fit. The
265 thickness of the single leaflet of the PG was measured using the one-dimensional statistical
266 function tool, which computes the average height density across the image frame (or selected
267 area). The height density graph was plotted with their characteristic two peaks. Then, Gaussian
268 functions were fitted on each peak and the background peak was subtracted from the peak of
269 the non-background, to give the average height/thickness of the PG fragment.

270 AFM three-dimension (3D) image processing

271 The pseudo 3D AFM images in Fig. 1Aii-Eii, Fig. 2Eii (+ IPTG, -IPTG), and Fig. 3Eii-Fii,
272 were processed using Nanoscope analysis software. The following image processing
273 parameters were used; Pitch = 10, Z-axis aspect ratio = 0.3, image rotation = 0°, plot type =
274 height, and projection = parallel.

275 Fibre detection and orientation quantification

276 Peptidoglycan fibres in AFM images were detected and quantified using automated image
277 analysis methods. Our framework was implemented as a Matlab GUI, which accepts outputs
278 from Gwyddion or open-source alternatives such as TopoStats (43). In the first stage, we
279 upsampled all images to a uniform resolution (0.1 nm/pixel) to ensure uniformity of analyses
280 across samples. Flattening using a Difference of Gaussians (DoG) filter removed low spatial-
281 frequency components, separating the high spatial-frequency PG fibre network from the overall
282 geometry of the cell wall. Individual PG fibres were segmented by employing a ridge-detection
283 algorithm (44), the results of which were then fused into a continuous network using a
284 Watershed algorithm (45) to remove small gaps between fibres at crossing points. This rough
285 network was then skeletonised and converted to a graph consisting of nodes, representing fibre-
286 fibre crossing points, linked by edges, representing fibre bodies. This graph-based network was
287 then cleaned based on its topology, removing disconnected fibre sections and fusing adjacent
288 T-shaped configurations of fibres to more accurately capture X-shaped fibre-fibre crossings.
289 Edges and nodes were then assigned to separate fibres based on the original segmentation of
290 the fibre network. Finally, we measured the local orientation of fibres by considering each point
291 along the length of the fibre in turn, performing a linear regression on the points assigned to
292 the fibre within a neighbourhood of 10 pixels of the query point and used the resulting
293 regression slope as the orientation measurement. From these local orientation measurements,
294 we computed the angular histogram for each image. The fibreFinder codes are publicly
295 available (46).

296 Pore analysis and quantification using Fiji

297 To calculate the area of the pores distributed across both the inner and outer section of the PG,
298 we used a custom-made semi-automated pore analysis macro (AFM_Slicer) in an open-source
299 software ImageJ/FIJI (42). Firstly, the macro pre-filtered the high-resolution image by
300 downscaling the pixel number and removing the noise of the image using the despeckle tool in
301 FIJI. Next, the treated image was simultaneously binarized and sliced into stacks of binary
302 slices where black represented the fibres in the image and white denoted the pores. Lastly, the
303 area of the pores in each slice was calculated using the analyze particle tool, followed by

calculation of the cumulative fraction of the pore area in each slice. The slice for each image that had the maximum number of pores was used for the graphs in figs. S2, S6 and S10 (47).

Measurement of (p)ppGpp levels

S. aureus strains were grown overnight in low-phosphate CDM (39) at 37°C. Cultures were diluted to an OD₆₀₀ of 0.1 and grown for 2.5 h prior to the addition of 3.7 MBq of [³²P]H₃PO₄ and incubation for a further 3 h at 37°C. Cultures were subsequently normalized for optical density, cells recovered by centrifugation (17,000 × g for 5 min) and suspended in 100 µl of 600 mM formic acid. Cells were subjected to three freeze/thaw cycles and debris removed by centrifugation (17,000 × g for 5 min) before the lysate was filtered through a 3 kDa spin column. Ten microliters were subsequently spotted on PEI-cellulose F thin-layer chromatography (TLC) plates (Merck Millipore), nucleotides separated, and TLC plates developed using a 1.5 M KH₂PO₄, pH 3.6, buffer. The radioactive spots were visualized using an FLA 7000 Typhoon PhosphorImager, and data were quantified using ImageQuantTL software.

Cell volume measurements

The cell volume measurements from the microscopy images were performed using a semi-automatic analysis approach (CocciVol) with a combination of FIJI macros (available at <https://github.com/Laia-Pasquina/CocciVol>) and a user-friendly machine learning interactive open-source software named ilastik (48). First the raw data from the confocal Nikon microscope was obtained in a file format .nd2. The raw data contains a stack of 11 slices across 3 µm with the cells focused approximately on the middle with a minimum of three channels: ADA-DA, NHS-ester and brightfield. The *Macro1_V2_Filtering_preparing_image.ijm* file in GitHub opens the raw image and creates a Z stack from the NHS-ester channel of 3 slices around the focus (which needs to be pre-determined by the user by opening the image with FIJI and manually finding the focus). Then, the image in .png format is processed in ilastik using two projects. The first ilastik project uses machine learning to run a pixel segmentation routine to learn from the users input in a few cells and then classify the rest of the cells in what pixels correspond to cells and what pixels are background. The second ilastik project uses an object classification routine similar to the first one but that classifies the cells into good fit or bad fit for volume analysis as well as applying some watershed filters to distinguish cells that are too close together (like diploids). Finally, the ilastik program outputs a table with the analysis of several physical parameters for each cell, which requires further processing to obtain the volume of the cells. This additional processing is carried out with *Macro2_Calculate_Volume_from_table.ijm* in FIJI (42) to obtain an Excel table with each cell number, volume and the ratio between the short axis and the long axis of the cell. Once one image was analysed for one type of sample there is a batch processing option in ilastik which was used to process an average of 5 images per sample. Using this approach, n = 600 images can be analysed in 30 min or less and a similar number of cells were analysed for each sample. Several samples were compared to each other in this manuscript. The CocciVol approach was used for the graphs in figs. S4, S5 & S9 (49).

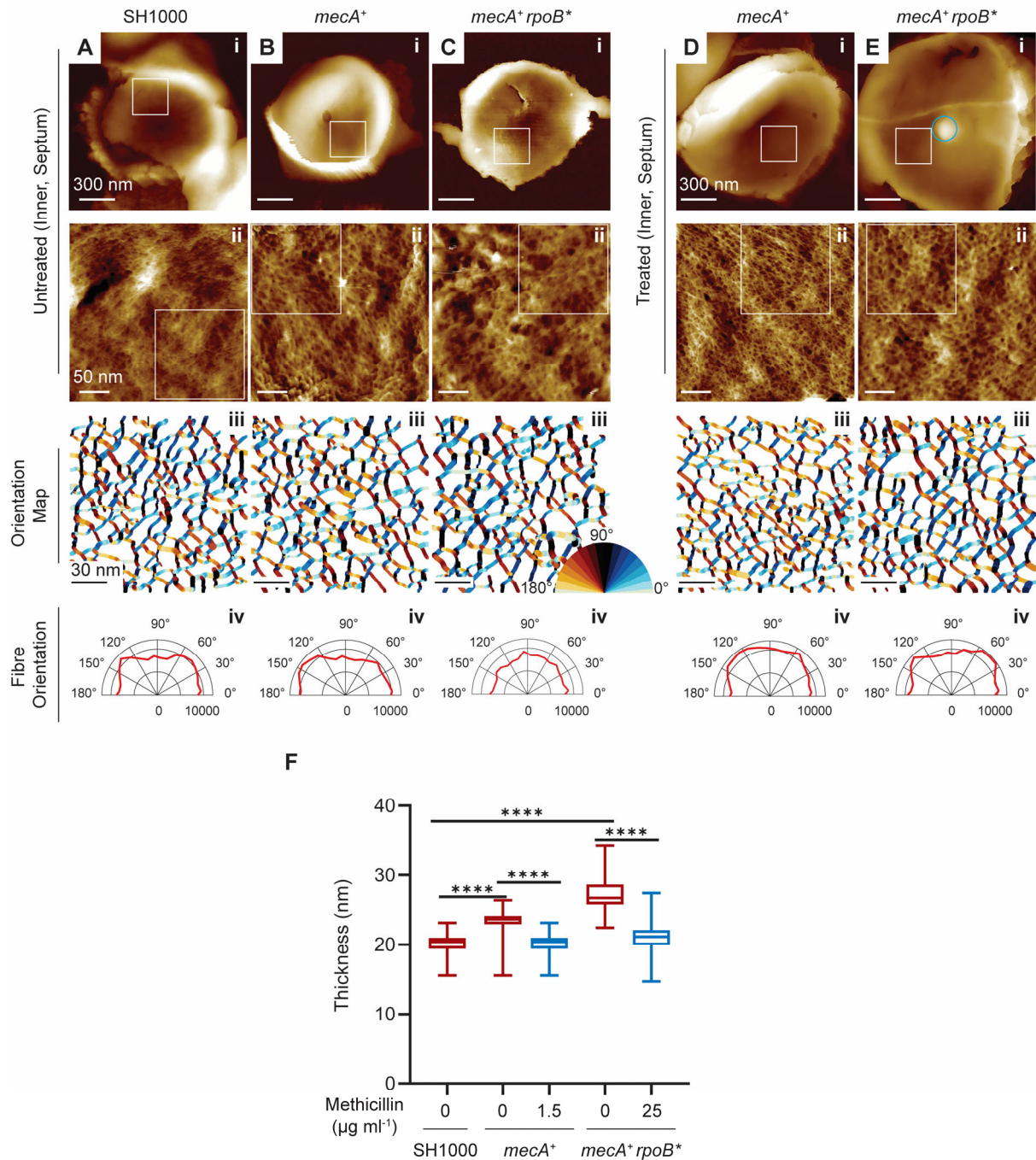


Fig. S1.

Effect of methicillin on the PG architecture of the inner surface of the septum in MRSA. (A-F) Parental MSSA strain, SH1000 (A) and MRSA strains, *mecA*⁺ (B, D) and *mecA*⁺ *rpoB*^{*} (C, E) were grown without (Untreated; A-C) or with methicillin (Treated; D, E), at 1.5 and 25 $\mu\text{g ml}^{-1}$ for D and E respectively. (i) AFM images of the inner surface of the septum and (ii) corresponding higher resolution topographic images of the selected location marked with white square in (i). The topographical height (z) range is as follows; (Ai) 230 nm, (Aii) 13 nm, (Bi) 420 nm, (Bii) 11 nm, (Ci) 170 nm, (Cii) 13.5 nm, (Di) 545 nm, (Dii) 11.5 nm, (Ei) 520 nm, (Eii) 8 nm. The circle in (E) indicates the presence of a cell wall lump which is a characteristic feature of *mecA*⁺ *rpoB*^{*} when treated with methicillin. The minimum height of the lump is 10 nm (n = 10, hydrated sacculi). (iii) Represents the colour-coded orientation map of the fibre

chains detected within the white box in (ii), and (iv) depicts the angular histogram of combined orientation of three independent AFM images. The image analysis method used for glycan orientation detection is described in the Materials and Methods section. (F) Plot of the measured thickness of dehydrated sacculi of SH1000, *mecA*⁺ and *mecA*⁺ *rpoB*^{*} with respect to without (red) and with methicillin treatment (light blue). The thickness data were compared using the Mann-Whitney test (****, $P < 0.0001$, $n = 28$ for each strain and condition). Data are representative of three independent biological repeats.

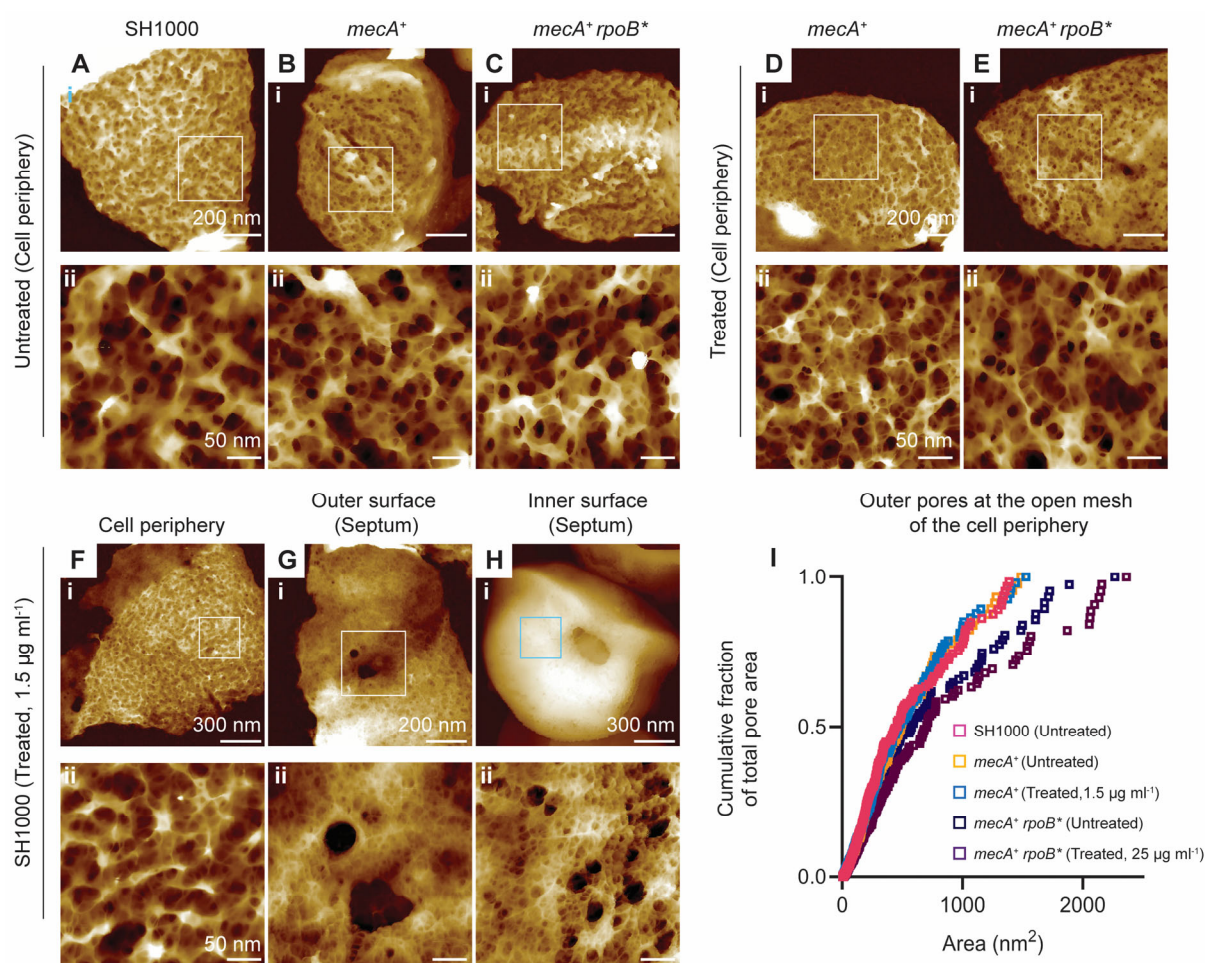


Fig. S2.

Effect of methicillin on the PG architecture of the cell periphery of MRSA strains. (A-C) The parental MSSA strain, SH1000 ((A) and MRSA strains, *mecA*⁺ (B) and *mecA*⁺ *rpoB*^{*} (C) were grown without (Untreated; A-C) or with methicillin (Treated; D, E), at 1.5 and 25 $\mu\text{g ml}^{-1}$ for D and E, respectively. (i) AFM images of the outer open mesh of the cell wall periphery and (ii) corresponding higher resolution topographic images of the selected location marked with white square in (i). The topographical height (*z*) range is as follows; (Ai) 80 nm, (Aii) 33 nm, (Bi) 110 nm, (Bii) 45 nm, (Ci) 140 nm, (Cii) 48 nm, (Di) 100, (Dii) 35 nm, (Ei) 95 nm, (Eii) 45 nm. (F-H) AFM images of (i), low resolution and (ii) corresponding higher resolution topographic images of the selected location marked with white square in (i) of sacculi of SH1000 treated 1.5 $\mu\text{g ml}^{-1}$ methicillin. (F) Outer PG mesh at the cell periphery; (G) Outer surface of the septum; (H) Inner surface of the septum. The topographical height (*z*) range is as follows; (Fi) 70 nm, (Fii) 35 nm, (Gi) 95 nm, (Gii) 43 nm, (Hi) 950 nm, (Hii) 48 nm. (I) Combined plot of cumulative fraction of total pore area, distributed over the outer open mesh shown in (A-E) (ii). Data are representative of three independent biological repeats and five AFM-independent images.

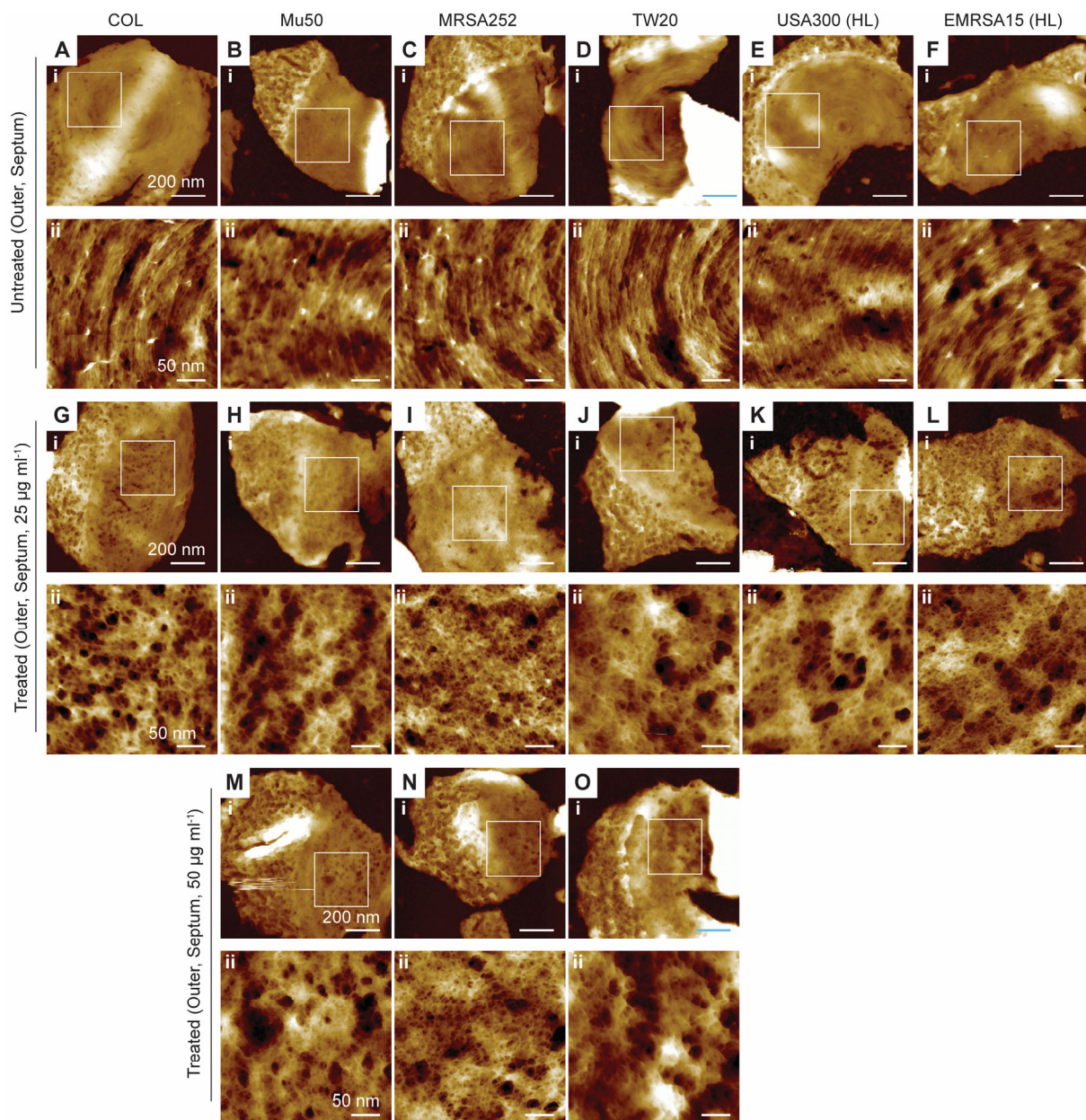


Fig. S3.

AFM characterization of high level resistant clinical strains. (A-F) Show AFM topographic images of the outer surfaces of newly revealed septa in samples of isolated sacculi of untreated (A) COL, (B) Mu50, (C) MRSA252, (D) TW20, (E) USA300(HL), and (F) EMRSA15(HL). (i) Low-resolution AFM images and (ii) corresponding higher-resolution images of the region indicated by the white boxes in (i). The topographical height (z) range is as follows; (Ai) 150 nm, (Aii) 13.5 nm, (Bi) 85 nm, (Bii) 11 nm, (Ci) 75 nm, (Cii) 9 nm, (Di) 65 nm, (Dii) 11.5 nm, (Ei) 80 nm, (Eii) 13.5 nm, (Fi) 105 nm, and (Fii) 11.5 nm. (G-L) Show outer surfaces of the septa of the same strains treated with 25 µg ml⁻¹ methicillin. (i) Low-resolution AFM images and (ii) corresponding higher-resolution images of the region indicated by the white boxes in (i). The topographical height (z) range is as follows; (Gi) 95 nm, (Gii) 16 nm, (Hi) 90 nm, (Hii) 18 nm, (Ii) 65 nm, (Iii) 12 nm, (Ji) 88 nm, (Jii) 24 nm, (Ki) 60 nm, (Kii) 25 nm, (Li) 65 nm, and (Lii) 35 nm. (M-O) Show the outer surface of the newly revealed septa of Mu50, MRSA252, and TW20 treated with 50 µg ml⁻¹ methicillin. (i) Low-resolution AFM images and (ii) corresponding higher-resolution images of the region indicated by the white boxes in (i).

396 The topographical height (z) range is as follows; (**Mi**) 130 nm, (**Mii**) 36 nm, (**Ni**) 105 nm, (**Nii**)
397 24 nm, (**Oi**) 78 nm, and (**Oii**) 28 nm. Data are representative of two independent biological
398 repeats and three AFM-independent images.

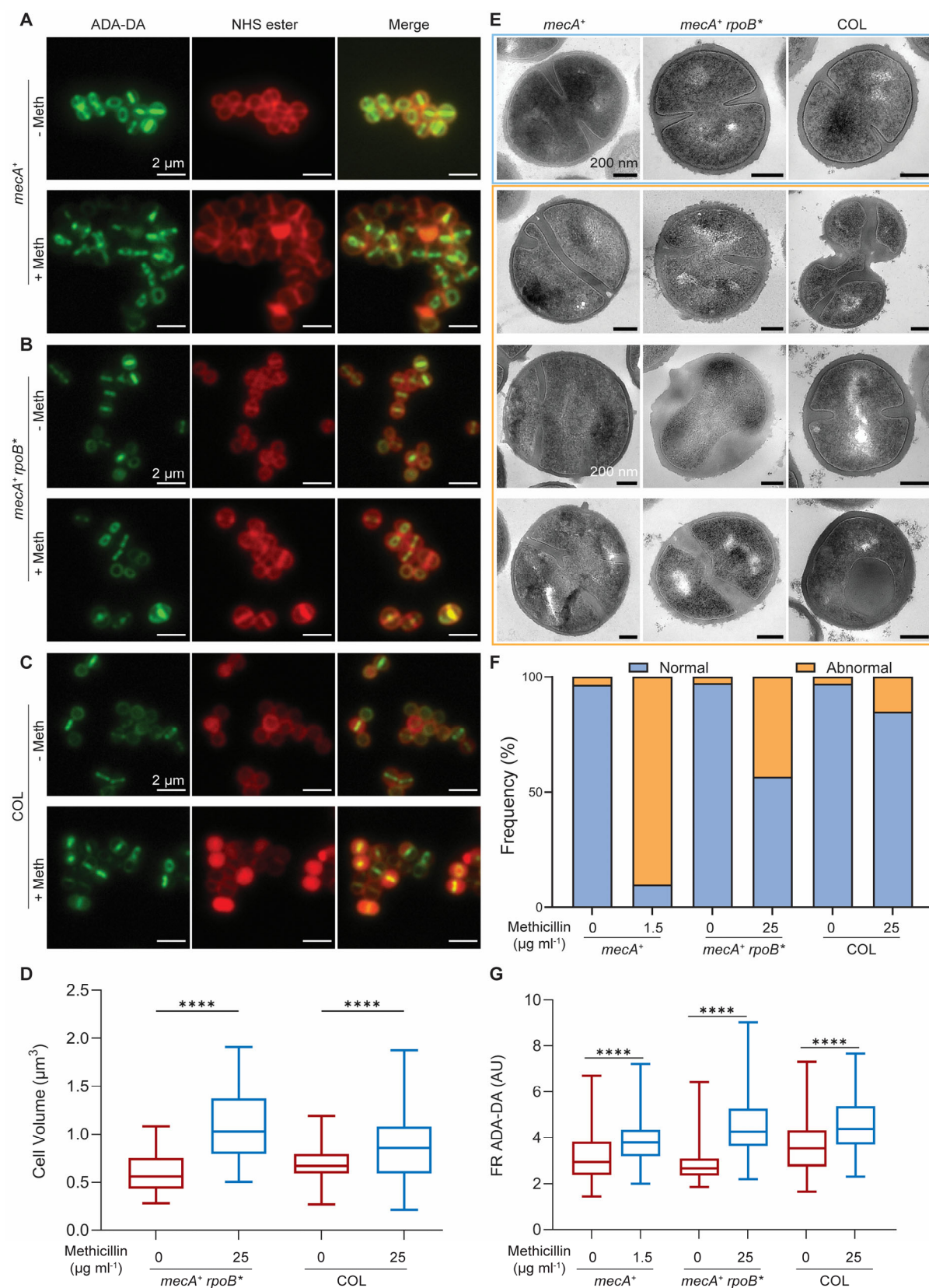


Fig. S4.

Effect of methicillin on cell morphology of MRSA strains. (A-C) Fluorescence microscopy images of ADA-DA and NHS-ester labelled MRSA strains (A) *mecA*⁺, (B) *mecA*⁺ *rpoB*⁺, and (C) COL grown without (-Meth, i) or with methicillin (+Meth, ii), at 1.5, 25 and 25 $\mu\text{g ml}^{-1}$

for **A**, **B** and **C**, respectively. (**D**) Cell volumes of *mecA*⁺ *rpoB*^{*} and COL without and with methicillin (1.5 µg ml⁻¹ and 25 µg ml⁻¹), as measured by fluorescence microscopy after NHS-ester Alexa Fluor 555 labelling. The *P* value was determined by Mann-Whitney U tests (****, *P* < 0.0001). The number of cells analysed per sample was *n* ≥ 300. (**E**) Shows TEM images of *mecA*⁺, *mecA*⁺ *rpoB*^{*} and COL grown with methicillin at 1.5, 25 and 25 µg ml⁻¹ respectively. Representatives of cells with normal septa are within a light blue frame while cells with abnormal septa are within orange frame. (**F**) Quantification of cellular phenotypes based on TEM. Cells were categorised as normal and abnormal, depending on the presence of a misplaced, multiple or misshapen septa or other cell cycle defects. Scale bar = 200 nm. Data are representative of two independent biological repeats (*n* ≥ 300). (**G**) Fluorescence ratio (FR) was calculated by dividing the fluorescence intensity at the septum by the intensity at the cell periphery of *mecA*⁺, *mecA*⁺ *rpoB*^{*}, and COL grown without (red, 0 µg ml⁻¹) and with methicillin (light blue) at different concentrations 1.5, 25 and 25 µg ml⁻¹ respectively. Differences are highly significant (*****P* < 0.0001) with higher FR for cells treated with methicillin (light blue) compared to no treatment (red). Higher values indicate more PG incorporation at the septum whilst lower values mean more peripheral PG. Number of cells analysed for each sample was 100.

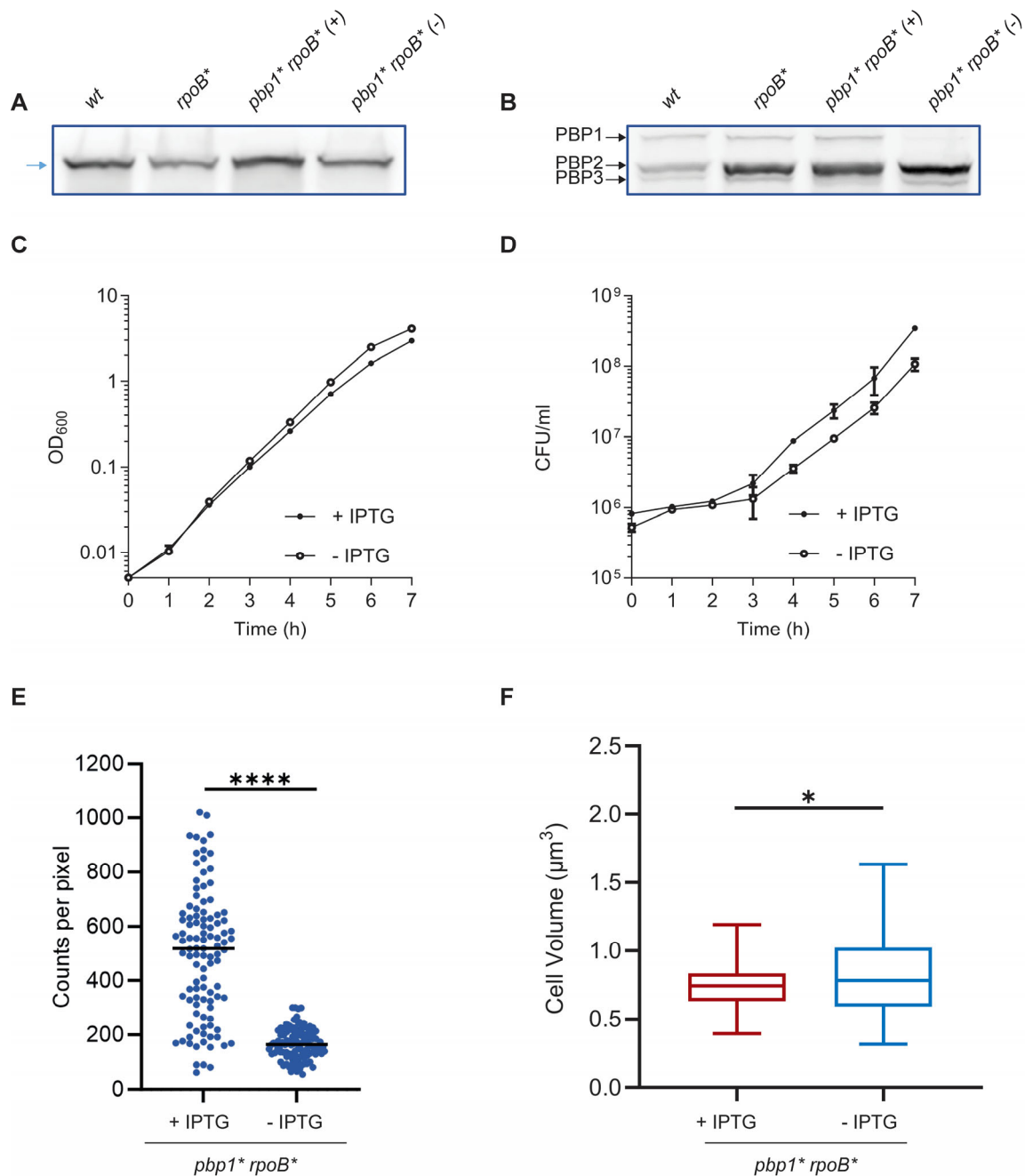


Fig. S5.

Analysis of the role of PBP1 transpeptidase activity. (A) Immunoblot of whole cell lysates of SH1000, *rpoB** and *pbp1* rpoB** grown with IPTG (+) without IPTG (-) for 4 h analysed using anti-PBP1 antibody. Expected PBP1 and PBP1* size = 83 kDa (blue arrowhead). (B) BocillinFL gel-based analysis of PBPs in SH1000, *rpoB** and *pbp1* rpoB** grown with IPTG (+) without IPTG (-) for 4 h; the locations of PBPs on the blots are indicated (arrows). (C) Growth curves of *pbp1* rpoB** grown in the presence or absence of IPTG (+ IPTG and - IPTG, respectively). Data represent the mean \pm SD. Error bars that are smaller than the data point symbols are not shown. (D) CFU counts of *pbp1* rpoB** grown in the presence or absence of IPTG (+ IPTG and - IPTG, respectively). Data represent the mean \pm SD. Error bars that are smaller than the data point symbols are not shown. (E) ADA-DA, clicked to Atto488, incorporation over 5 min in *pbp1* rpoB** (SJF5306) grown with IPTG (+) and without IPTG (-). Fluorescence intensities were compared using a one-way ANOVA with Tukey's multiple

435 comparison test (****, $P < 0.0001$). Number of cells analysed for each sample was $n = 110$.
436 Each dot represents a single cell. A black line indicates the median of each distribution. Data
437 are representative of three independent biological repeats. (F) Cell volumes of *pbpI** *rpoB**
438 after incubation with (+, red, average cell volume is $0.75 \pm 0.16 \mu\text{m}^3$) or without (-, light blue,
439 average cell volume is $0.83 \pm 0.30 \mu\text{m}^3$) IPTG for 4h, as measured by fluorescence microscopy
440 after NHS-ester Alexa Fluor 555 labelling. The P value was determined by Mann-Whitney U
441 tests (*, $P = 0.0266$). Number of cells analysed for each sample was ≥ 250 .

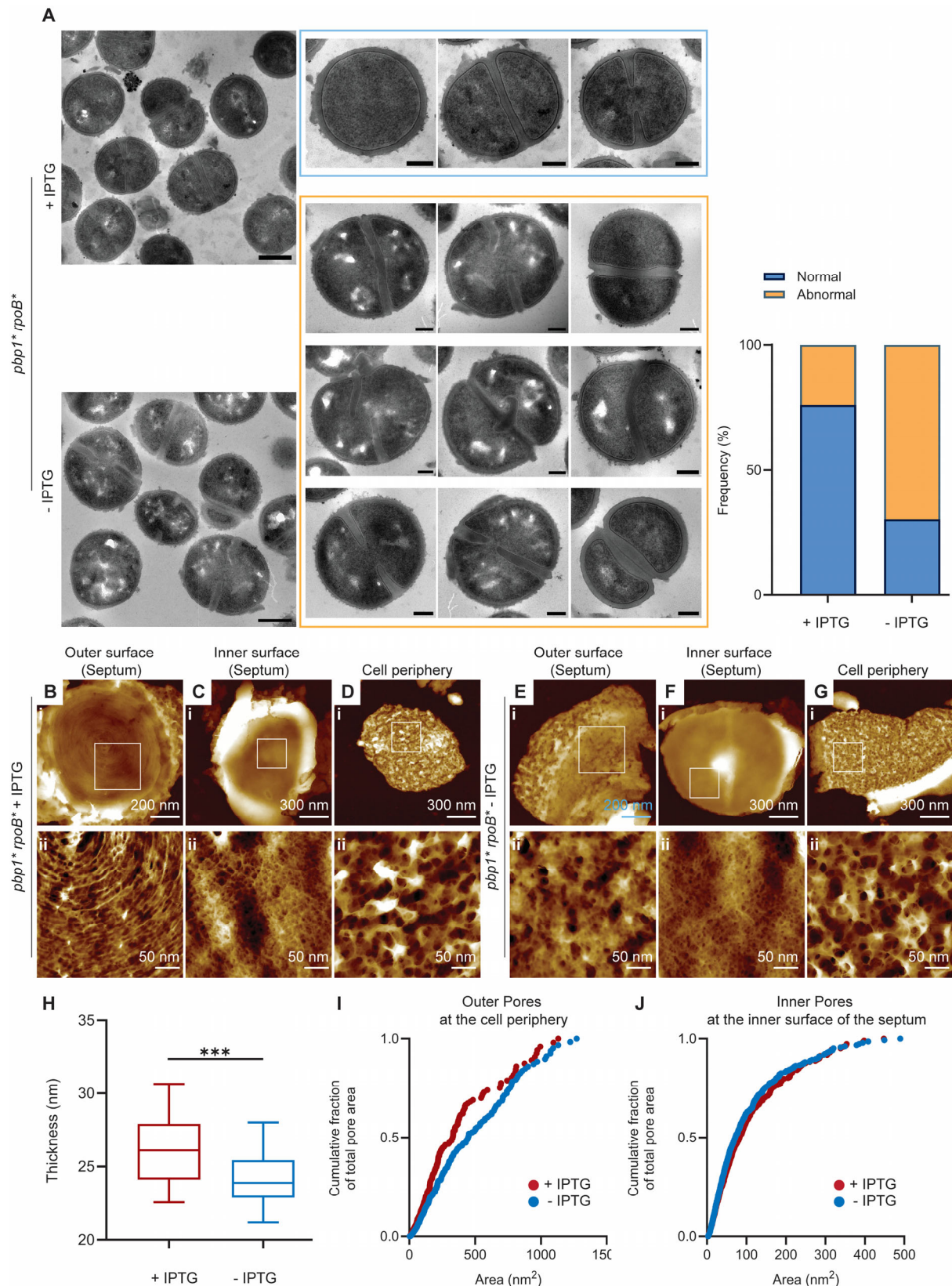


Fig. S6.

Cell wall morphology of *pbp1* rpoB** revealed by TEM and AFM. (A) Left, representative TEM micrographs of *pbp1* rpoB** grown for 4 h in the presence and absence of IPTG. Scale bars = 500 nm. Examples of cells classified as normal and abnormal phenotypes are shown

447 within the light blue (+IPTG) and orange frames (-IPTG), respectively. Scale bar = 200 nm.
 448 TEM data are representative of two independent biological repeats with $n \geq 300$ per
 449 sample. Right, quantification of cellular phenotypes associated with *pbpl** *rpoB**, based on
 450 the TEM data. **(B-G)** AFM images of the outer surface of the septum (**B**, **E**), the inner surface
 451 of the septum (**C**, **F**), and the open mesh at the cell periphery (**D**, **G**) associated with *pbpl**
 452 *rpoB** grown in the presence of IPTG (+ IPTG; **B-D**) and absence of IPTG (- IPTG; **E-G**). For
 453 **(B-G)** (i) are individual fragments of sacculus and (ii) are higher resolution topographic AFM
 454 images of the selected location marked with the white square in (i). The topographical height
 455 (z) range is as follows; + IPTG: 120 nm (**Bi**), 8.5 nm (**Bii**), 270 nm (**Ci**), 13 nm (**Cii**), 120 nm
 456 (**Di**), 55 nm (**Dii**). -IPTG: 110 nm (**Ei**), 22 nm (**Eii**), 290 nm (**Fi**), 17 nm (**Fii**), 120 nm (**Gi**), 48
 457 nm (**Gii**). Data are representative of three independent biological repeats and more than 10
 458 AFM independent imaging experiments. **(H)** Plot of the measured thickness of dehydrated
 459 sacculi of *pbpl** *rpoB** after incubation with (+, red) or without (-, light blue) IPTG for 4h.
 460 The number of independent fragments measured for each strain was 20. The *P* value was
 461 determined by Mann-Whitney U tests (***, $P = 0.0009$). **(I-J)** Cumulative fraction of total pore
 462 area as a function of the area of the pores distributed across the open mesh surface of the cell
 463 wall periphery surface (**I**) and the inner surface (**J**) of the septum of *pbpl** *rpoB** grown in the
 464 presence of IPTG (+ IPTG, red) and absence of IPTG (- IPTG, light blue).

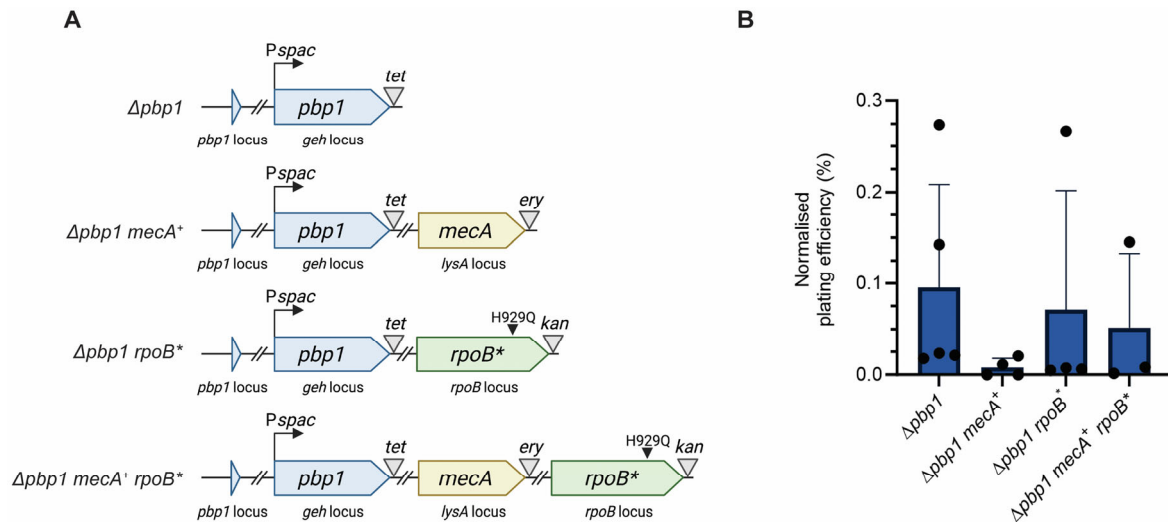


Fig. S7.

Analysis of the role of PBP1 in growth. **(A)** Schematic representation of the $\Delta pbp1$ genetic constructs. An ectopic copy of *pbp1* was placed under the control of the *Pspac* promoter at the lipase (*geh*) locus, while the gene in the native *pbp1* locus was deleted ($\Delta pbp1$). In $\Delta pbp1\ mecA^+$ and $\Delta pbp1\ mecA^+ rpoB^*$ a copy of a *mecA*⁺ gene under the control of its native promoter is placed at the *lysA* locus. In $\Delta pbp1\ rpoB^*$ and $\Delta pbp1\ mecA^+ rpoB^*$, the *rpoB* gene has a point mutation which results in a single amino acid replacement (H929Q) in RNA polymerase β subunit (*rpoB*^{*}). *tet*, *ery* and *kan* represent tetracycline, erythromycin and kanamycin resistance cassettes, respectively. The graphics were created with BioRender.com. **(B)** Plating efficiency of the SH1000 derivatives $\Delta pbp1$, $\Delta pbp1\ mecA^+$, $\Delta pbp1\ rpoB^*$ and $\Delta pbp1\ mecA^+ rpoB^*$ in the absence of IPTG. Plating efficiency values were compared with the control groups grown in the presence of IPTG. Data were compared using a one-way ANOVA with Dunnett's multiple comparison test (ns, not significant, $P \geq 0.05$, $n \geq 3$). Data represent the mean \pm SD.

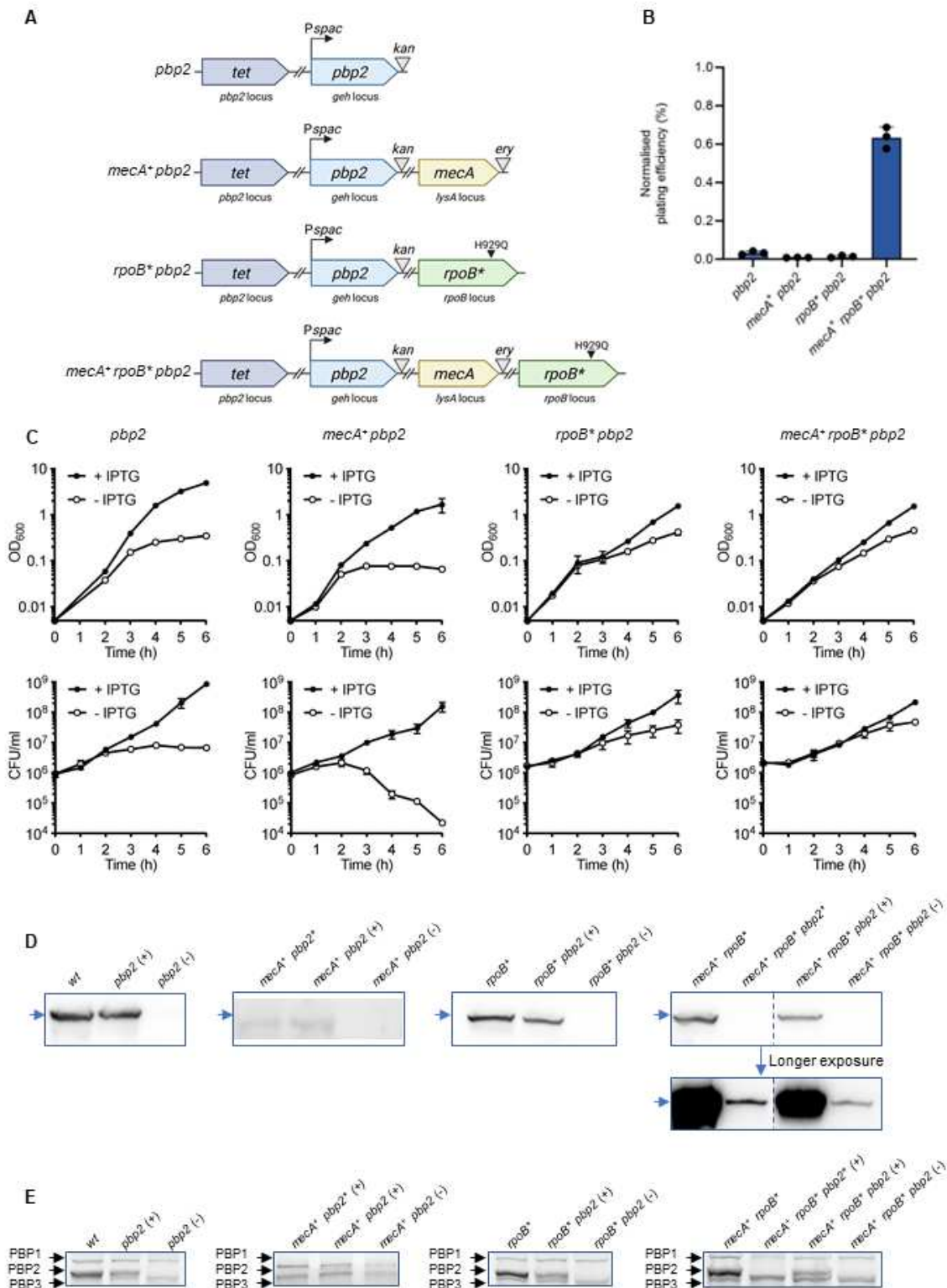


Fig. S8.

Analysis of the role of PBP2 in growth. (A) Schematic representation of the *pbp2* genetic constructs. An ectopic copy of *pbp2* was placed under the control of the Pspac promoter at the SH1000 lipase (*geh*) locus, while the gene in the native *pbp2* locus was deleted (marked with *tet*). In *mecA*⁺ *pbp2* and *mecA*⁺ *rpoB*⁺ *pbp2* a copy of a *mecA* gene expressed from its native

promoter was located at the *lysA* locus. In *rpoB** *pbp2* and *mecA⁺ rpoB** *pbp2* the *rpoB* gene has a point mutation which results in a single amino acid change (H929Q) in the RNA polymerase β subunit (*rpoB**). The graphics were created with BioRender.com. **(B)** Plating efficiency of the derivatives *pbp2*, *mecA⁺ pbp2*, *rpoB** *pbp2* and *mecA⁺ rpoB** *pbp2* grown in the absence of IPTG. Plating efficiency values were compared with the control groups grown in the presence of IPTG. Data represent the mean \pm SD. **(C)** Growth curves of SH1000 derivatives *pbp2*, *mecA⁺ pbp2*, *rpoB** *pbp2*, and *mecA⁺ rpoB** *pbp2* grown in the presence or absence of IPTG (+ IPTG and - IPTG, respectively). Data represent the mean \pm SD. Error bars that are smaller than the data point symbols are not shown. **(D)** Immunoblots, analysed using anti-PBP2 antibody, of whole cell lysates of SH1000 (wt) and *mecA⁺ rpoB**, *rpoB**, *pbp2*, *mecA⁺ pbp2*, *rpoB** *pbp2* and *mecA⁺ rpoB** *pbp2* derivatives grown in the presence (+) or absence (-) of IPTG for 4 h. *mecA⁺ pbp2** and *mecA⁺ rpoB** *pbp2** were grown in the presence of IPTG throughout. Expected PBP2 and PBP2* sizes = 80 kDa are indicated (blue arrowhead). **(E)** BocillinFL gel-based analysis of PBPs in SH1000 and *mecA⁺ rpoB**, *rpoB**, *pbp2*, *mecA⁺ pbp2*, *rpoB** *pbp2*, and *mecA⁺ rpoB** *pbp2* grown in the presence (+) or absence (-) of IPTG for 4 h. *mecA⁺ pbp2** and *mecA⁺ rpoB** *pbp2** were grown in the presence of IPTG throughout. Data are representative of two **(D and E)** and three **(B and C)** independent biological experiments.

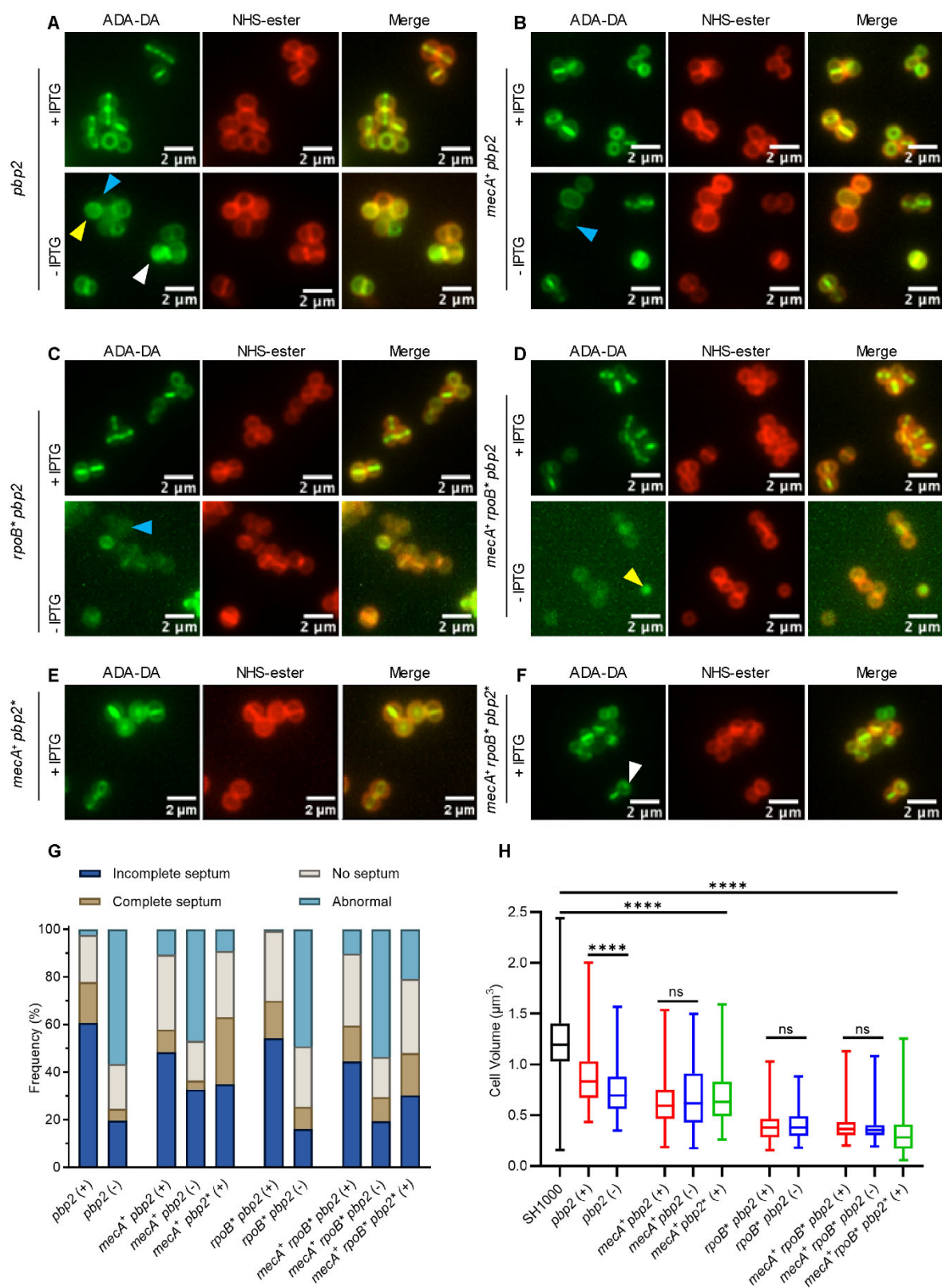


Fig. S9.

Role of PBP2 in cell morphology. (A-F) Fluorescence microscopy images of the SH1000 derivatives *pbp2* (A), *mecA⁺ pbp2* (B), *rpoB^{*} pbp2* (C) and *mecA⁺ rpoB^{*} pbp2* (D) grown in

507 the presence (+ IPTG) or absence (- IPTG) of the inducer for 4 h. *mecA*⁺ *pbp2** (**E**) and *mecA*⁺
508 *rpoB** *pbp2** (**F**) were grown in the presence of IPTG at all times. All strains were incubated
509 for 5 min with ADA-DA clicked to Atto488 to show nascent PG, and counter labelled with
510 NHS-ester Alexa Fluor 555 to image the cell wall. Images are average intensity projections of
511 z stacks. Cells with dispersed, apparent ADA-DA incorporation (yellow arrowheads), no ADA-
512 DA incorporation (blue arrowheads) or mislocalized ADA-DA incorporation (white
513 arrowheads) are examples of cells that were classified as abnormal in panel **G**. (**G**)
514 Quantification of cellular phenotypes based on ADA-DA incorporation in **A-F**. From left to
515 right, *n* = 247, 235, 261, 288, 237, 273, 299, 309, 278 and 305. (**H**) Cell volumes of strains in
516 **A-F** measured by fluorescence microscopy after NHS-ester Alexa Fluor 555 labelling. Number
517 of cells analysed for each sample was *n* ≥ 300. Data are representative of three independent
518 biological experiments.

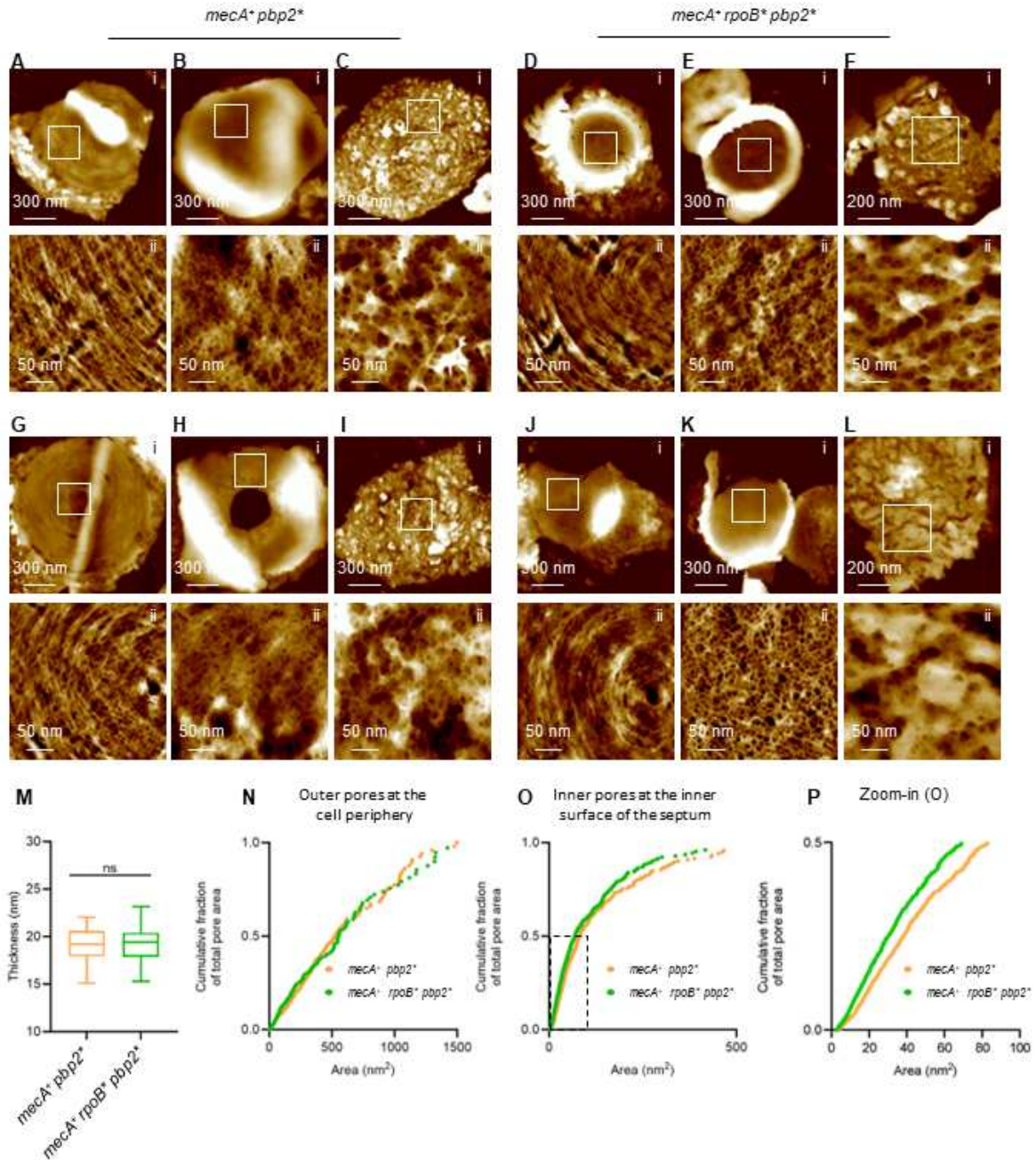


Fig. S10.

Surface-dependent nanoscale architecture of *mecA*⁺ *pbp2*^{*} and *mecA*⁺ *rpoB*^{*} *pbp2*^{*} revealed by AFM. AFM topographic images of the outer surface of the septum (A), the inner surface of the septum (B), and open mesh structure of the cell periphery (C) associated with the cell wall of *mecA*⁺ *pbp2*^{*}. (i) Low-resolution AFM images and (ii) corresponding higher-resolution images of the region indicated by the white boxes in (i). Topographical height (z) range for (i) are 100 nm, 330 nm, and 85 nm and for (ii) are 11 nm, 16 nm, and 45 nm respectively. (D-F) AFM images of the same cell wall locations for *mecA*⁺ *rpoB*^{*} *pbp2*^{*}; (i) and (ii) as above. The height scales for (i) are 200 nm, 140 nm, and 130 nm. The height scales for (ii) are 16 nm, 9 nm, and 55 nm respectively. (G-I) AFM images of the PG structures associated with the following locations on the cell wall of *mecA*⁺ *pbp2*^{*}; (G) AFM images of the outer surface of the septum, (H) inner surface of an incomplete septum, and (I) open mesh structure of the cell

532 periphery; (i) and (ii) as above. Topographical heights (z) for (i) are 150 nm, 210 nm, and 85
533 nm. Topographical heights (z) for (ii) are 11 nm, 22 nm, and 51 nm respectively. **(J-L)** AFM
534 images of PG structures of the same locations in *mecA⁺ rpoB* pbp2**; (i) and (ii) as above.
535 Topographical heights (z) for (i) are 140 nm, 200 nm, and 130 nm and for (ii) are 12 nm, 14
536 nm, and 70 nm respectively. **(M)**, Plot of the measured thickness of dehydrated sacculi of
537 *mecA⁺ pbp2** and *mecA⁺ rpoB* pbp2** respectively. The number of independent fragments
538 measured for each strain was 20. Data were analysed using the Mann-Whitney non-parametric
539 statistical test (ns, not significant = 0.7180). **(N-O)** Cumulative fraction of total pore area as a
540 function of the area of the pores distributed across the open mesh surface of the cell wall
541 periphery surface **(N)** and the inner surface **(O)** of the septum of *mecA⁺ pbp2** and *mecA⁺*
542 *rpoB* pbp2**. **(P)** Zoomed-in plot of the region highlighted by the dashed box in **(O)**. Data are
543 representative of two independent biological repeats and five AFM independent images.

Strain	Oxacillin MIC ($\mu\text{g ml}^{-1}$)	Methicillin MIC ($\mu\text{g ml}^{-1}$)
SH1000 (SJF682)	≤ 0.25	0.5
<i>mecA</i> ⁺ (SJF4996)	2	4
<i>mecA</i> ⁺ <i>rpoB</i> [*] (SJF5003)	> 256	> 256
COL (SJF315)	> 256	> 256
Mu50 (SJF5041)	> 256	> 256
MRSA252 (SJF4821)	> 256	> 256
TW20 (SJF6101)	> 256	> 256
USA300 (SJF4703)	0.75	1-2
USA300 (HL) (SJF6109)	> 256	64-128
EMRSA 15 (SJF6025)	16-24	64
EMRSA15 (HL) (SJF6110)	> 256	> 256
<i>geh::mecA</i> ⁺ (SJF5324)	4-8	-
<i>geh::mecA</i> ⁺ <i>rpoB</i> [*] (SJF5323)	> 256	-
<i>mecA</i> ⁺ <i>lytH</i> (SJF5461)	12	-
<i>mecA</i> ⁺ <i>gdpP</i> (SJF5464)	≤ 2	-
<i>mecA</i> ⁺ <i>pde2</i> (SJF5460)	3	-
<i>mecA</i> ⁺ <i>rel</i> [*] (SJF5463)	> 256	-
<i>mecA</i> ⁺ <i>clpP</i> (SJF5459)	12-16	-
<i>mecA</i> ⁺ <i>clpX</i> (SJF5462)	6-8	-
<i>rpoB</i> [*] (SJF5010)	≤ 0.25	-
<i>lytH</i> (SJF5455)	≤ 0.5	-
<i>gdpP</i> (SJF5025)	≤ 0.5	-
<i>pde2</i> (SJF5454)	≤ 0.125	-
<i>rel</i> [*] (SJF5457)	≤ 0.5	-
<i>clpP</i> (SJF5453)	0.25	-
<i>clpX</i> (SJF5456)	0.25-0.38	-

545 **Table S1.**

546 Oxacillin and Methicillin MICs for *S. aureus* strains. The MICs for oxacillin and methicillin
547 were determined using E-test strips or the microdilution method (respectively) in triplicate as
548 described in Materials and Methods. -, Not determined.

Strain	Genotype and Markers	Source
<i>Escherichia coli</i>		
NEB5 α	<i>fhuA2 (argF-lacZ)U169 phoA glnV44 80 (lacZ)M15 gyrA96 recA1 relA1 endA1 thi-1 hsdR17</i>	New England Biolabs
<i>Staphylococcus aureus</i>		
SH1000	Functional <i>rsbU</i> ⁺ derivative of <i>S. aureus</i> 8325-4	(50)
COL	Healthcare acquired MRSA (HA-MRSA)	(51)
Mu50	HA-MRSA	(19)
MRSA252	HA-MRSA	(18)
TW20	HA-MRSA	(17)
USA300	Community-acquired MRSA (CA-MRSA)	(20)
USA300 (HL) (SJF6109)	High-level oxacillin resistant derivative of USA300	This study
EMRSA 15	CA-MRSA	(3)
EMRSA15 (HL) (SJF6110)	High-level oxacillin resistant derivative of EMRSA15	This study
VF17	SH1000 pGL485 (<i>lacI</i>); Cm ^R	(34)
RN4220	Restriction deficient transformation recipient	(52)

CYL316	RN4220 pCL112Δ19; Cm ^R	(53)
SJF4924	SH1000 <i>geh::Pspac-pbp2</i> , Kan ^R	This study
SJF5046	SH1000 <i>lysA::mecA rpoB^{H929Qkan}</i> ; Ery ^R , Kan ^R	(14)
<i>pbp1</i> * (SJF4656)	SH1000 <i>geh::Pspac-pbp1</i> <i>pbp1::pbp1* lacI</i> ; Tet ^R , Cm ^R	(8)
<i>pbp1</i> * <i>mecA</i> ⁺ (SJF5223)	SH1000 <i>geh::Pspac-pbp1</i> <i>pbp1::pbp1* lacI lysA::mecA</i> ; Tet ^R , Cm ^R , Ery ^R	(8)
<i>pbp1</i> * <i>rpoB</i> * (SJF5306)	SH1000 <i>geh::Pspac-pbp1</i> <i>pbp1::pbp1* lacI rpoB^{H929Qkan}</i> ; Tet ^R , Cm ^R , Kan ^R	This study
<i>pbp1</i> * <i>mecA</i> ⁺ <i>rpoB</i> * (SJF5226)	SH1000 <i>geh::Pspac-pbp1</i> <i>pbp1::pbp1* lacI lysA::mecA</i> <i>rpoB^{H929Qkan}</i> ; Tet ^R , Cm ^R , Ery ^R , Kan ^R	(8)
Δ <i>pbp1</i> (SJF5106)	SH1000 <i>geh::Pspac-pbp1 Δpbp1 lacI</i> ; Tet ^R , Cm ^R	(8)
Δ <i>pbp1</i> <i>mecA</i> ⁺ (SJF5224)	SH1000 <i>geh::Pspac-pbp1 Δpbp1 lacI</i> <i>lysA::mecA</i> ; Tet ^R , Cm ^R , Ery ^R	(8)
Δ <i>pbp1</i> <i>rpoB</i> * (SJF5305)	SH1000 <i>geh::Pspac-pbp1 Δpbp1 lacI</i> <i>rpoB^{H929Qkan}</i> ; Tet ^R , Cm ^R , Kan ^R	This study
Δ <i>pbp1</i> <i>mecA</i> ⁺ <i>rpoB</i> * (SJF5227)	SH1000 <i>geh::Pspac-pbp1 Δpbp1 lacI</i> <i>lysA::mecA rpoB^{H929Qkan}</i> ; Tet ^R , Cm ^R , Ery ^R , Kan ^R	(8)
<i>pbp2</i> (SJF5630)	SH1000 <i>geh::Pspac-pbp2 pbp2::tet</i> <i>lacI</i> ; Tet ^R , Kan ^R , Cm ^R	This study

<i>mecA</i> ⁺ (SJF4996)	SH1000 <i>lysA::mecA</i> ; Ery ^R	(14)
<i>mecA</i> ⁺ <i>rpoB</i> [*] (SJF5003)	SH1000 <i>lysA-mecA rpoB</i> ^{H929Q} ; Ery ^R	(14)
<i>rpoB</i> [*] (SJF5010)	SH1000 <i>lysA::kan rpoB</i> ^{H929Q} ; Kan ^R ,	(14)
<i>mecA</i> ⁺ <i>pbp2</i> (SJF5663)	SH1000 <i>lysA::mecA geh::Pspac-pbp2 pbp2::tet lacI</i> ; Ery ^R , Kan ^R , Tet ^R , Cm ^R	This study
<i>mecA</i> ⁺ <i>rpoB</i> [*] <i>pbp2</i> (SJF5674)	SH1000 <i>lysA::mecA rpoB</i> ^{H929Q geh::Pspac-pbp2 pbp2::tet lacI; Ery^R, Kan^R, Tet^R, Cm^R}	This study
GMSA015	SH1000 <i>lysA::ery</i> ; Ery ^R	(54)
<i>rpoB</i> [*] <i>pbp2</i> (SJF5690)	SH1000 <i>lysA::ery rpoB</i> ^{H929Q geh::Pspac-pbp2 pbp2::tet lacI; Ery^R, Kan^R, Tet^R, Cm^R}	This study
<i>mecA</i> ⁺ <i>pbp2</i> [*] (SJF5807)	SH1000 <i>lysA::mecA geh::Pspac- pbp2* pbp2::tet lacI</i> ; Ery ^R , Kan ^R , Tet ^R , Cm ^R	This study
<i>mecA</i> ⁺ <i>rpoB</i> [*] <i>pbp2</i> [*] (SJF5809)	SH1000 <i>lysA::pmecA rpoB</i> ^{H929Q geh::Pspac-pbp2*(TP-) pbp2::tet lacI; Ery^R, Kan^R, Tet^R, Cm^R}	This study
<i>geh::mecA</i> ⁺ <i>rpoB</i> [*] (SJF5323)	SH1000 <i>geh::mecA lysA::tet rpoB</i> ^{H929Q} ; Kan ^R , Tet ^R	(14)
<i>geh::mecA</i> ⁺ (SJF5324)	SH1000 <i>geh::mecA lysA::tet</i> ; Kan ^R , Tet ^R	(14)
NE1369	JE2 <i>lytH::Tn</i> ; Ery ^R	(55)
<i>lytH</i> (SJF5455)	SH1000 <i>lytH::Tn</i> ; Ery ^R	This study

<i>mecA</i> ⁺ <i>lytH</i> (SJF5461)	SH1000 <i>geh::mecA lysA::tet lytH::Tn</i> ; Kan ^R , Tet ^R , Ery ^R	This study
ANG1959	SEJ1 <i>gdpP::kan</i>	(56)
<i>gdpP</i> (SJF5025)	SH1000 <i>gdpP::kan</i>	This study
<i>mecA</i> ⁺ <i>gdpP</i> (SJF5464)	SH1000 <i>lysA::mecA gdpP::kan</i> ; Ery ^R Kan ^R ,	This study
NE1208	JE2 <i>pde2::Tn</i> ; Ery ^R	(55)
<i>pde2</i> (SJF5454)	SH1000 <i>pde2::Tn</i> ; Ery ^R	This study
<i>mecA</i> ⁺ <i>pde2</i> (SJF5460)	SH1000 <i>geh::mecA lysA::tet pde2::Tn</i> ; Kan ^R , Tet ^R , Ery ^R	This study
NE1714	JE2 <i>rel::Tn</i> ; Ery ^R	(55)
<i>rel</i> (SJF5457)	SH1000 <i>rel::Tn</i> ; Ery ^R	This study
<i>mecA</i> ⁺ <i>rel</i> (SJF5463)	SH1000 <i>geh::mecA lysA::tet rel::Tn</i> ; Kan ^R , Tet ^R , Ery ^R	This study
<i>pbpI</i> * <i>rel</i> (SJF5513)	SH1000 <i>geh::Pspac-pbpI</i> <i>pbpI::pbpI* lacI rel::Tn</i> ; Tet ^R , Cm ^R , Ery ^R	This study
<i>clpP</i> SJF5453)	SH1000 <i>clpP::Tn</i> ; Ery ^R	This study
<i>mecA</i> ⁺ <i>clpP</i> (SJF5459)	SH1000 <i>geh::mecA, clpP::Tn</i> ; Ery ^R Kan ^R	This study
<i>clpX</i> (SJF5456)	SH1000 <i>clpX::Tn</i> ; Ery ^R	This study
<i>mecA</i> ⁺ <i>clpX</i> (SJF5462)	SH1000 <i>geh::mecA, clpX::Tn</i> ; Ery ^R Kan ^R	This study

NE912	JE2 <i>clpP::Tn; Ery^R</i>	(55)
SJF1704	8325-4 <i>clpX::Tn; Ery^R</i>	Lab stock

550 **Table S2.**

551 Strains used in this study.

552 Cm^R – chloramphenicol, Ery^R – erythromycin, Kan^R – kanamycin, Tet^R – tetracycline

Name	Characteristics	Source
pCQ11-FtsZ-SNAP	pCQ11 derivative containing <i>ftsZ-snap</i> under Pspac; Amp ^R , Ery ^R	(57)
pGM074	pKASBAR-kan derivative with <i>ezrA-psmorange</i> ; Amp ^R , Tet ^R	(54)
pKB-Pspac- <i>pbp2</i>	pGM074 derivative containing Pspac, <i>S. aureus pbp2</i> RBS and full length <i>pbp2</i> ; Amp ^R , Kan ^R	This study
pKB-Pspac- <i>pbp2*</i>	pGM074 derivative containing Pspac, <i>S. aureus pbp2</i> RBS and full length <i>pbp2</i> with inactivated TP (<i>pbp2*</i>); Amp ^R , Kan ^R	This study
pMAD	<i>E. coli-S. aureus</i> shuttle vector with temperature-sensitive origin of replication in <i>S. aureus</i> and constitutively produced thermostable β -galactosidase encoded by <i>bgaB</i> ; Amp ^R , Ery ^R	(58)
pMAD- $\Delta pbp2$	pMAD containing a deletion cassette for <i>S. aureus pbp2</i> ; Amp ^R , Ery ^R . Tet ^R	This study
pAISH1	TetR derivative of pMUTIN4; Amp ^R ; Tet ^R	(54)

553 **Table S3.**

554 Plasmids used in this study. Amp^R – ampicillin, Ery^R – erythromycin, Kan^R – kanamycin, Tet^R
555 – tetracycline

Name	Sequence 5'–3'
pCQ11-pbp2-F	agaaggagatatatacatatggagtgaggaccgcgtatgac
pCQ11-pbp2-R	atttattatgcatttagaataggtagttgaatataacctgttaatccac
pKB-pbp2-R	cagctatgaccatgattacgtagttgaatataacctgttaatccac
pKB-Pspac-pbp1-F	ccttttttgccccgggatccgcaaaaagttgttgactttatc
pbp2TP-F	ccctactggtggatctttaaacc
pbp2TP-R	tgaggatctgttgcttg
pMAD- Δ pbp2-F	ccatggtacccgggagctcgacgatgaaaatacttttaataataaaaatc
pbp2-up-R	acactatctgcaggtcatacgcggtcctcac
tetR-pbp2-F	gaccgcgtatgacctgcagatagtgtacgtaaaaag
tetR-pbp2-R	tatgttgagtggactctctccaaagttgatc
pbp2-down-F	ctttgggagagagtccactcaacataaaatcctc
pMAD- Δ pbp2-R	ccatggtacccgggagctcgacgatgaaaatacttttaataataaaaatc

556 **Table S4.**

557 Oligonucleotides used in this study.